

CM²



MAGAZINE

第 62 期



南方科技大学海洋磁学中心主编

<https://cm2.sustech.edu.cn/>

创刊词

海洋是生命的摇篮，是文明的纽带。地球上最早的生命诞生于海洋，海洋里的生命最终进化成了人类，人类的文化融合又通过海洋得以实现。人因海而兴。

人类对海洋的探索从未停止。从远古时代美丽的神话传说，到麦哲伦的全球航行，再到现代对大洋的科学钻探计划，海洋逐渐从人类敬畏崇拜幻想的精神寄托演变成可以开发利用与科学研究的客观存在。其中，上个世纪与太空探索同步发展的大洋科学钻探计划将人类对海洋的认知推向了崭新的纬度：深海（deep sea）与深时（deep time）。大洋钻探计划让人类知道，奔流不息的大海之下，埋藏的却是亿万年的地球历史。它们记录了地球板块的运动，从而使板块构造学说得到证实；它们记录了地球环境的演变，从而让古海洋学方兴未艾。

在探索海洋的悠久历史中，从大航海时代的导航，到大洋钻探计划中不可或缺的磁性地层学，磁学发挥了不可替代的作用。这不是偶然，因为从微观到宏观，磁性是最基本的物理属性之一，可以说，万物皆有磁性。基于课题组的学科背景和对海洋的理解，我们对海洋的探索以磁学为主要手段，海洋磁学中心因此而生。

海洋磁学中心，简称 CM^2 ，一为其全名“Centre for Marine Magnetism”的缩写，另者恰与爱因斯坦著名的质能方程 $E = MC^2$ 对称，借以表达我们对科学巨匠的敬仰和对科学的不懈追求。

然而科学从来不是单打独斗的产物。我们以磁学为研究海洋的主攻利器，但绝不仅限于磁学。凡与磁学相关的领域均是我们关注的重点。为了跟踪反映国内外地球科学特别是与磁学有关的地球科学领域的最新研究进展，海洋磁学中心特地主办 CM^2 Magazine，以期与各位地球科学工作者相互交流学习、合作共进！

“海洋孕育了生命，联通了世界，促进了发展”。21世纪是海洋科学的时代，由陆向海，让我们携手迈进中国海洋科学的黄金时代。

目 录

文献速递.....	1
1. 南大西洋异常的非单调增长和运动.....	1
2. 两万年来亚北极太平洋及其边缘海海表温度变化：古海洋综述.....	4
3. U-Pb 定年的挪威 Svalbard 钻孔的磁性地层揭示 M0r 开始时间为 121.2 ± 0.4 Ma.....	9
4. 氧同位素示踪地球最早陆壳的起源.....	12
5. 俯冲持续时间和板片倾斜.....	16
6. 气候稳定性定义的东亚季风区的全新世气候适宜期.....	19
7. 利用硅藻和生产力参数推断 172 ka 以来白令海西部的轨道和亚轨道环境变化.....	23
8. 第一个成冰纪的古强度结果及其对内核成核年龄的潜在意义.....	26
9. 洞穴沉积物记录了中心更新世格陵兰东北部温暖湿润的气候.....	29
10. 裂谷火山活动和埃迪卡拉末期生物灭绝的联系：来自墨西哥 Sonora 地区地层学及 U-Pb 年代学综合研究.....	34
11. 地球化学数据表明火星子午线平原的格拉斯伯格组和伯恩组地层的沉积物十分相似.....	36
12. 夏威夷近海淡水流的海洋电磁成像和体积估计.....	39

文献速递

1. 南大西洋异常的非单调增长和运动



翻译人：柳加波 liujb@sustech.edu.cn

Hagay A, Filipe T N, Maxime L, et al. *Non-monotonic growth and motion of the South Atlantic Anomaly*[J]. *Earth, Planets and Space (Online)*, 2021, 73(1).

<http://doi.org/10.1186/s40623-021-01356-w>

摘要：南大西洋异常（SAA）是地球表面磁场强度特别低的区域。准确表征 SAA 对于了解地核活动和地球动力学以及社会问题（例如破坏地面观测站和机载航天器的仪器）都非常重要。本文，我们提出了新的方法来更好地表征 SAA 范围和中心，包含了 SAA 区域外围的表面强度变化和形状各向异性。将这些表征应用于涵盖历史时期的地磁场模型中，我们发现 SAA 区域和中心具有很强的时间依赖性，包括稳定区域，向东漂移和快速向南漂移的时期。我们根据核-幔边界上相关的大规模地磁通量斑块的长期变化来解释这些特殊时期。我们的表征可以用作对类地发电机数值模型的约束。

ABSTRACT: The South Atlantic Anomaly (SAA) is a region at Earth's surface where the intensity of the magnetic field is particularly low. Accurate characterization of the SAA is important for both fundamental understanding of core dynamics and the geodynamo as well as societal issues such as the erosion of instruments at surface observatories and onboard spacecrafts. Here, we propose new measures to better characterize the SAA area and center, accounting for surface intensity changes outside the SAA region and shape anisotropy. Applying our characterization to a geomagnetic field model covering the historical era, we find that the SAA area and center are more time dependent, including episodes of steady area, eastward drift and rapid southward drift. We interpret these special events in terms of the secular variation of relevant large-scale geomagnetic flux patches on the core–mantle boundary. Our characterization may be used as a constraint on Earth-like numerical dynamo models.

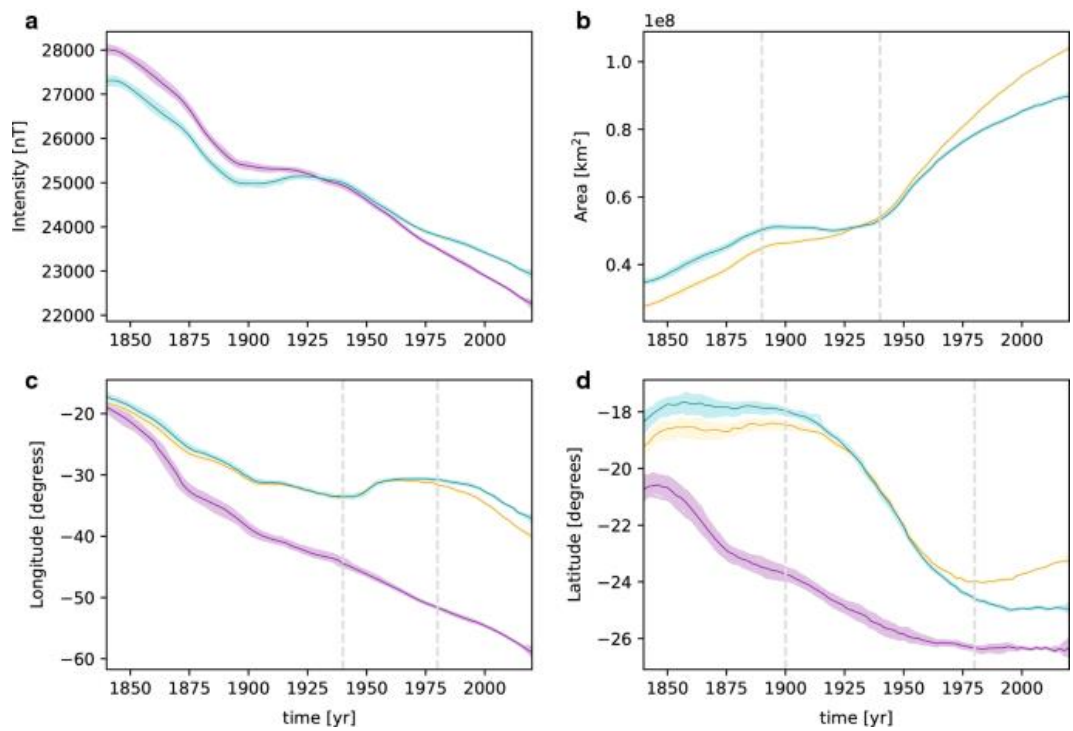


Figure 1. SAA characterization vs. time for the period 1840–2020. Dark lines denote the mean model of COV-OBS.x1, light envelopes denote the 100 realizations of the ensemble. a Minimum intensity (purple) and the relative minimum intensity $|B^*|_{\text{relmin}}|B \rightarrow \text{minrel}$ (turquoise). b Area based on S0 (yellow) and S1 (turquoise). c Longitude of center based on Min (purple), CM0 (yellow) and CM1 (turquoise). d Latitude of center based on Min (purple), CM0 (yellow) and CM1 (turquoise). Vertical dashed lines highlight special events of SAA area decrease (b), SAA center eastward drift (c) and SAA center rapid southward drift (d)

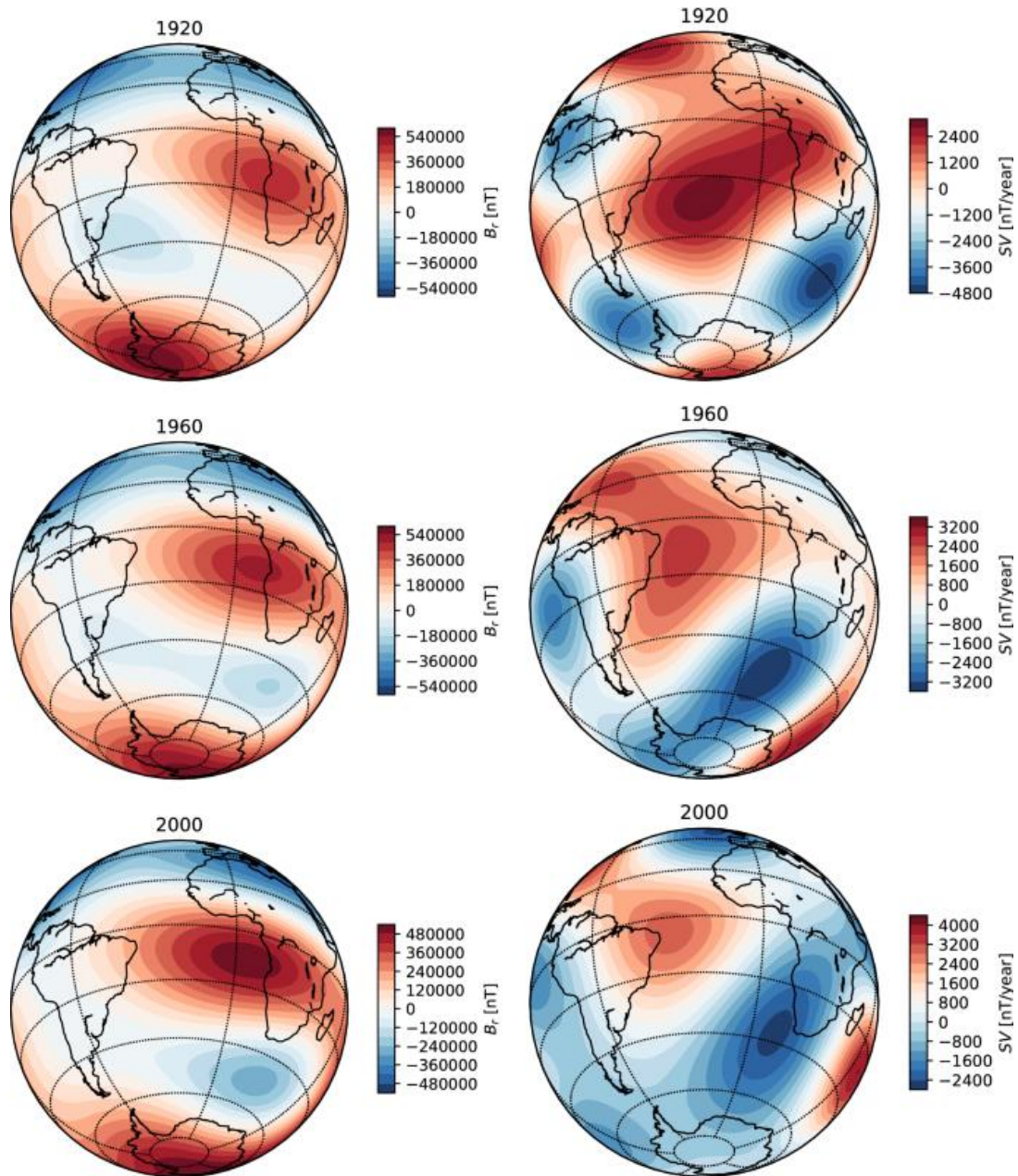


Figure 2. Radial geomagnetic field (left) and its secular variation (right) at the core–mantle boundary for the mean model of COV-OBS.x1 in 1920 (top), 1960 (middle) and 2000 (bottom). All models are expanded until spherical harmonic degree and order 5. All maps are centered at 20°W 20°W 30°S 30°S, i.e. on the South Atlantic. Note the different scales

2. 两万年来亚北极太平洋及其边缘海海表温度变化：古海洋综述



翻译人：仲义 zhongyi@sustech.edu.cn

Catherine, V. D., Sarah, E. M., Curtis, D., et al. *Sea surface temperature across the Subarctic North Pacific and marginal seas through the past 20,000 years: A paleoceanographic synthesis* [J] *Quaternary Science Reviews*, 2020, 246, 106519.

<https://doi.org/10.1016/j.quascirev.2020.106519>

摘要：冰消期以来亚北极太平洋及其边缘海的海洋表面状况是古海洋学研究的热点。然而，一直以来缺乏对近地表海洋学完整的途径，从而比较最后一次冰消时期区域间和区域内的变化。本文综合大量海表温度指标（有孔虫的 $\delta^{18}\text{O}$ 和 Mg/Ca 、颗石藻烯酮（ U^{k}_{37} ））涵盖了过去 20 ka 以来北太平洋及其边缘海的变化。结果显示，在末次冰期和冰消期时期，颗石藻烯酮（ U^{k}_{37} ）记录通常比附近有孔虫的 $\delta^{18}\text{O}$ 和 Mg/Ca 记录的海表温度显示更温暖，而在全新世时期海表温度表现一致。在鄂霍次克海，全新世有孔虫的 $\delta^{18}\text{O}$ 和 U^{k}_{37} 之间差别是由于近地表分层作用所导致的。作者发现在北太平洋及白令海地区，海表温度变暖趋势要早于 Bolling-Allerod (14.7 ka) 事件，且与全新世开始时期 (11.7 ka) 相一致。同时，指标记录也显示了与新仙女木事件 (12.9-11.7 ka) 同步变化。全新世开始后，西太平洋高纬度地区黑潮增强的影响明显，北太平洋环流强度的变化可能推动了海表温度东西向的跷跷板变化，这也是开放北太平洋间冰期的特征。

ABSTRACT: Deglacial sea surface conditions in the subarctic North Pacific and marginal seas are the subject of increasing interest in paleoceanography. However, a cohesive picture of near-surface oceanography from which to compare inter and intra-regional variability through the last deglaciation is lacking. We present a synthesis of sea surface temperature covering the open North Pacific and its marginal seas, spanning the past 20 ka using proxy records from foraminiferal calcite ($\delta^{18}\text{O}$ and Mg/Ca) and coccolithophore alkenones (U^{k}_{37}). Sea surface temperature proxies tend to

be in agreement through the Holocene, though $U^{k'}_{37}$ records are often interpreted as warmer than adjacent $\delta^{18}O$ or Mg/Ca records during the Last Glacial Maximum and early deglaciation. In the Sea of Okhotsk, Holocene discrepancies between $\delta^{18}O$ and $U^{k'}_{37}$ may be the result of changes in near-surface stratification. We find that sea-surface warming occurred prior to the onset of the Bølling-Allerød (14.7 ka) and coincident with the onset of the Holocene (11.7 ka) in much of the North Pacific and Bering Sea. Proxy records also show a cold reversal roughly synchronous with the Younger Dryas (12.9-11.7 ka). After the onset of the Holocene, the influence of an intensified warm Kuroshio Current is evident at higher latitudes in the Western Pacific, and an east-west seesaw in sea surface temperature, likely driven by changes in the strength of the North Pacific Gyre, characterizes the open interglacial North Pacific.

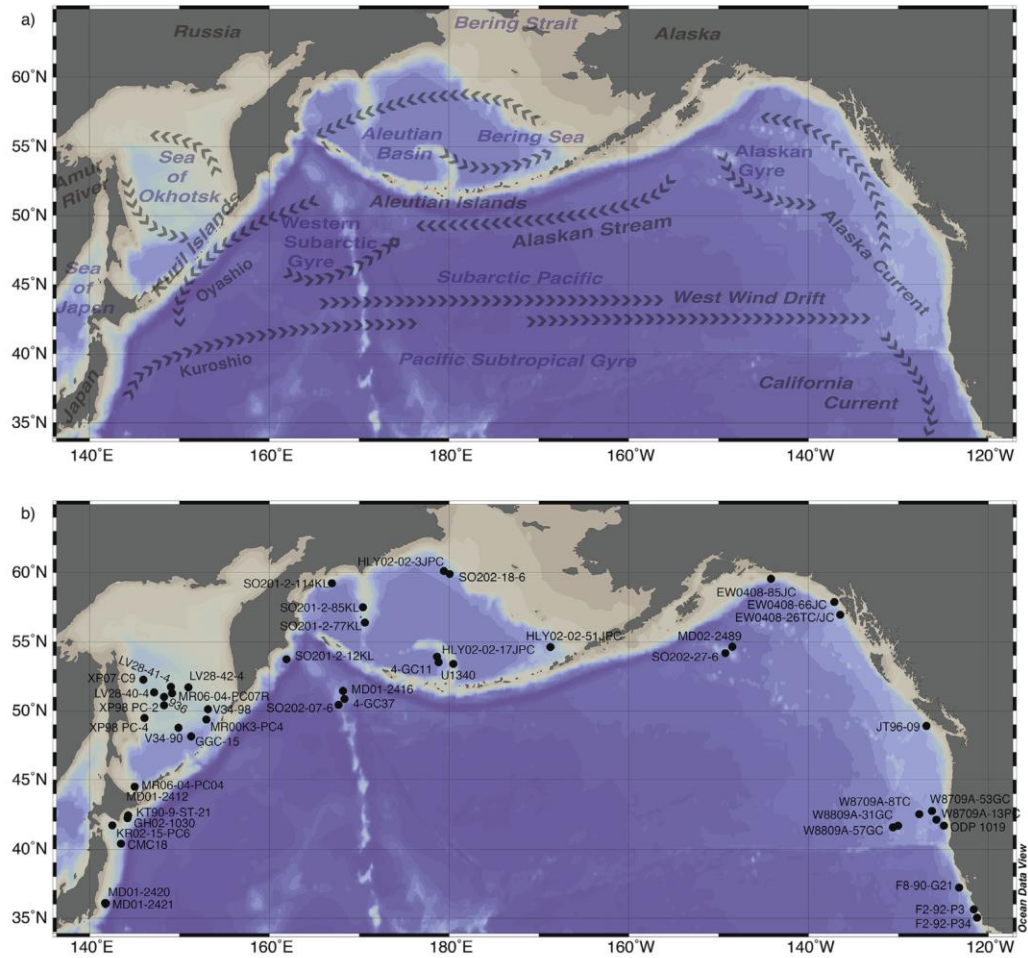


Figure 1. Schematic of the North Pacific demonstrating a) the general location and direction of the major surface currents of the North Pacific and marginal seas with the location of named currents after the Drifter-Derived Climatology of Global Near-Surface Currents (Laurindo et al., 2017) and b) core locations for all records included in this synthesis.

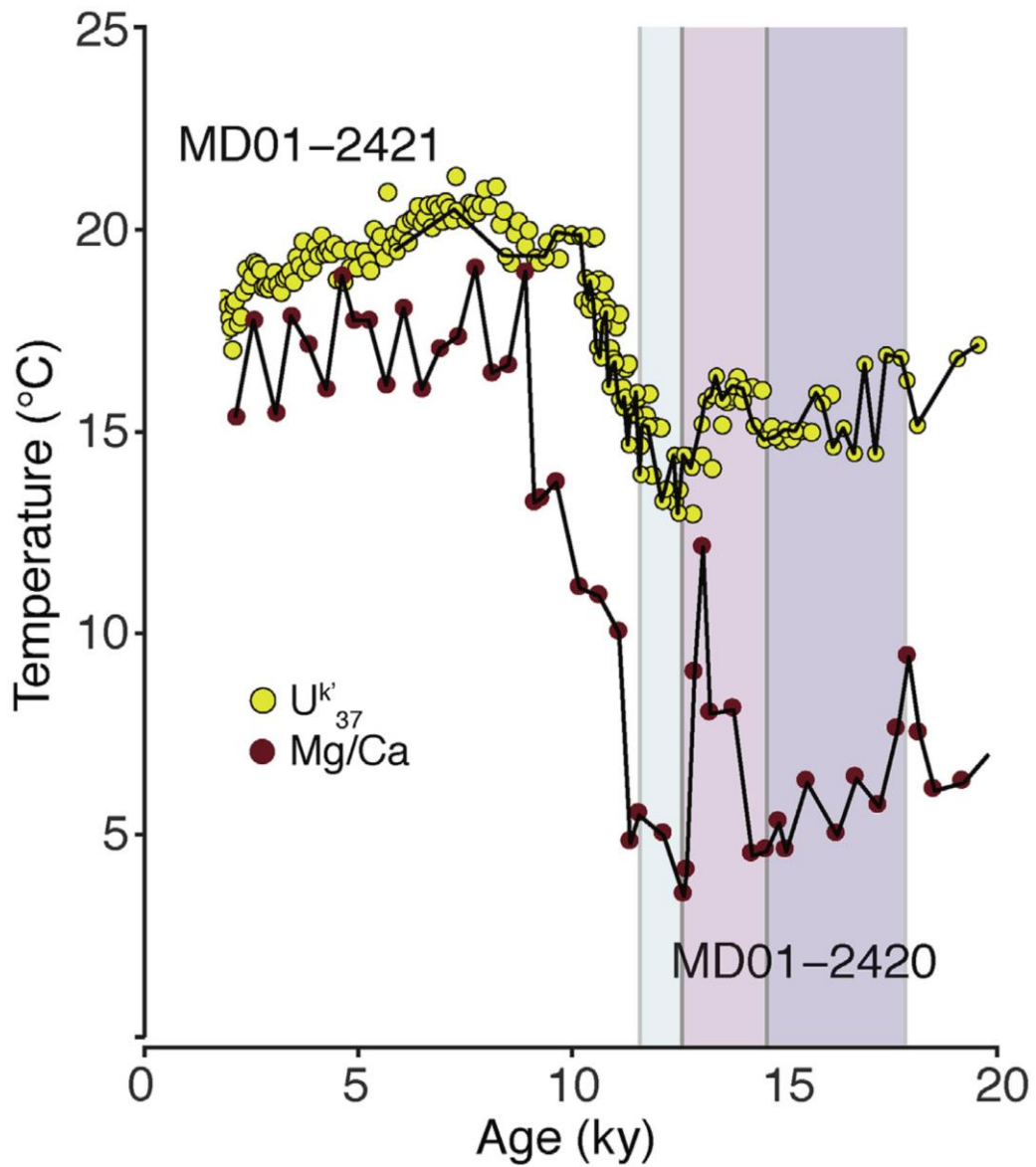


Figure 2. Comparison of U^{k}_{37} (yellow) and Mg/Ca (red) SST records from MD01-2421 and MD01-2420 respectively in the Western North Pacific. Purple shading denotes the Heinrich Stadial 1 Interval, pink the Bølling-Allerød, and blue the Younger Dryas from Greenland records. Both available U^{k}_{37} records for MD01-2420 have been included, although only the record reported by Yamamoto et al. (2004), with updated age model, has been connected with lines. (For interpretation of the references to color in this figure legend, the reader is referred to the Web version of this article.)

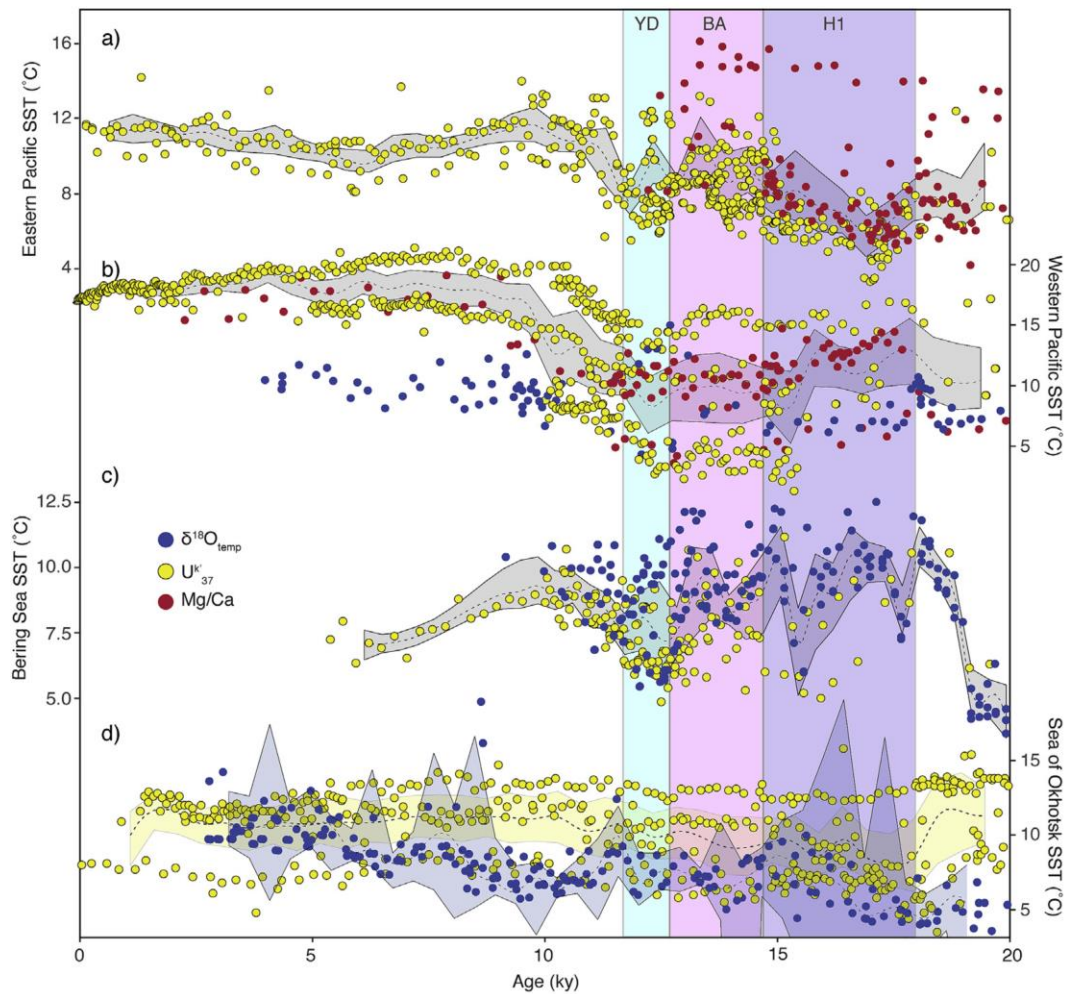


Figure 3. Comparison between SST trends in the a) Eastern North Pacific, b) Western North Pacific, c) the Bering Sea, and d) the Sea of Okhotsk. Broken lines in a-c show the trend in temperature, based on local regress ‘loess’ of all proxy types, with an envelope denoting the 95% bootstrap confidence interval. Individual data points are colored by proxy type. Purple shading denotes the Heinrich Stadial 1 Interval, pink the Bølling-Allerød, and blue the Younger Dryas from Greenland records. Records from the Sea of Okhotsk have been separate into temperature based upon $U^{k'}_{37}$ (yellow) or $\delta^{18}O_{temp}$ (blue) proxies. (For interpretation of the references to color in this figure legend, the reader is referred to the Web version of this article.

3. U-Pb 定年的挪威 Svalbard 钻孔的磁性地层揭示 M0r 开始时间为 121.2 ± 0.4 Ma



翻译人:李园洁 liyj3@sustech.edu.cn

Zhang Y, Ogg J G, Minguetz D, et al. *Magnetostratigraphy of U-Pb -dated boreholes in Svalbard, Norway, implies that magnetochron M0r (a proposed Barremian-Aptian boundary marker) begins at 121.2 ± 0.4 Ma*[J]. *Geology*, 2021.

<https://doi.org/10.1130/G48591.1>

摘要: 地磁极性时 M0r 的开始时间被认为是阿普特阶底部的标志,但是由于过去发表的放射性同位素年龄不一致和剖面地层对比的不确定性使得这个时间的确定存在争议。本文作者用挪威 Svalbar 的 DH1 岩芯的磁性地层校准一个膨润土, U-Pb 定年方法将 M1r 最上层定为 123.1 ± 0.3 Ma, 比 M0r 开始时间早 1.9 m.y.。这是第一次直接高精度放射性同位素定年校正到一个 M 序列的极性时。插值得到的 M0r 开始时间为 121.2 ± 0.4 Ma, 比 2012 地质年表年轻~5 my, 该年表的年龄是基于海洋玄武岩的放射性同位素定年和阿普特旋回地层插值得到的。校正后的年龄模型表明整个阿普特阶-圣通阶全球洋壳平均扩张速率相当于加快了~12%。今后可用放射性同位素定年和高分辨率旋回地层调查侏罗纪中期到白垩纪最早期哪个时间段增加了~4 my。

ABSTRACT: The age of the beginning of magnetic polarity Chron M0r, a proposed marker for the base of the Aptian Stage, is disputed due to a divergence of published radioisotopic dates and ambiguities in stratigraphic correlation of sections. Our magnetostratigraphy of core DH1 from Svalbard, Norway, calibrates a bentonite bed, dated by U-Pb methods to 123.1 ± 0.3 Ma, to the uppermost part of magnetozone M1r, which is ~1.9 m.y. before the beginning of Chron M0r. This is the first direct calibration of any high-precision radioisotopic date to a polarity chron of the M sequence. The interpolated age of 121.2 ± 0.4 Ma for the beginning of Chron M0r is younger by ~5 m.y. than its estimated age used in the Geologic Time Scale 2012, which had been extrapolated from

radioisotopic dates on oceanic basalts and from Aptian cyclostratigraphy. The adjusted age model implies a commensurate faster average global oceanic spreading rate of ~12% during the Aptian-Santonian interval. Future radioisotopic dating and high-resolution cyclostratigraphy are needed to investigate where to expand the mid-Jurassic to earliest Cretaceous interval by the required ~4 m.y.

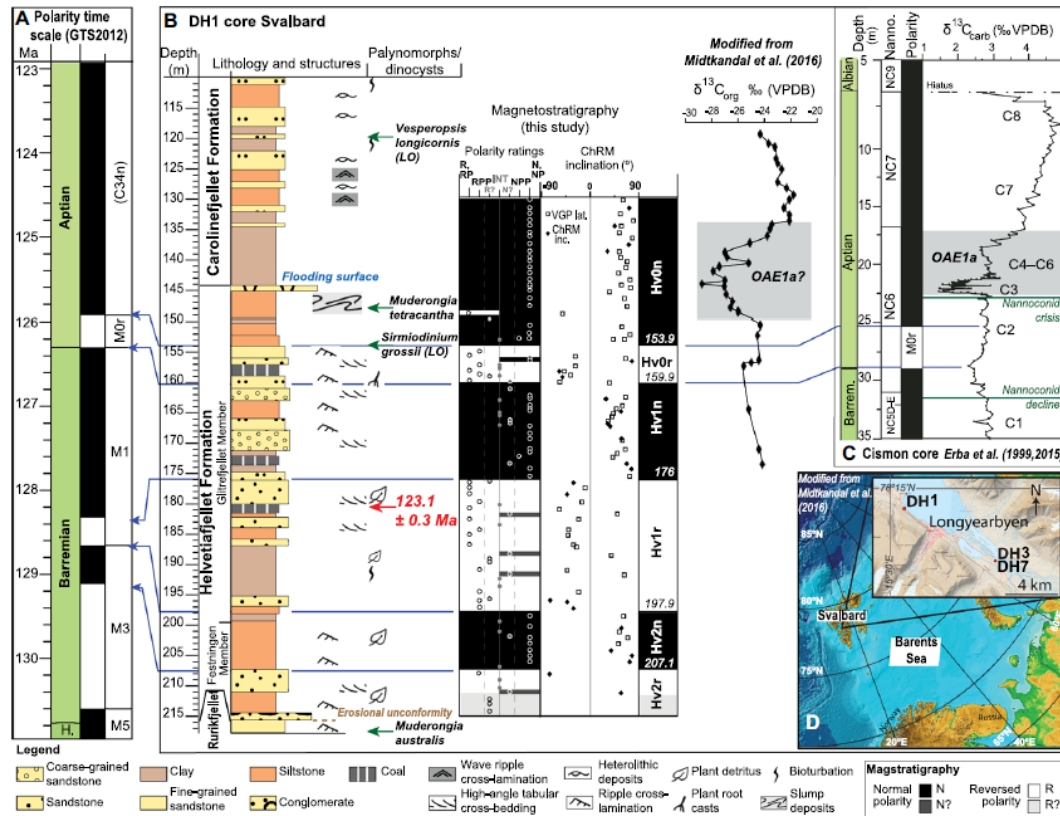


Figure 1. Magnetostratigraphy of Svalbard, Norway, borehole DH1 (drilled by Longyearbyen CO₂ Lab, <http://co2-ccs.unis.no/>) (B) and its correlation (blue lines) to the Geologic Time Scale 2012 (GTS2012) magnetic polarity scale (Gradstein et al., 2012) (A) in which the base of the Aptian Stage (set as base of Chron M0r) was placed at 126.3 Ma (H.—Hauterivian). Circles in the magnetostratigraphy represent the quality ratings (N, NP, NPP, etc.; see the Materials and Methods section) of magnetic polarity of each sample. Biostratigraphic constraints include palynomorphs of interpreted Barremian and Hauterivian ages and dinoflagellate cyst of Aptian age (*Vesperopsis longicornis*) (LO—last occurrence). Carbon-isotope curve from core DH1 (modified from Midtkandal et al., 2016) is compared to the Cismon core of Italy (C), which shows $\delta^{13}\text{C}_{\text{carb}}$ (carb—carbonate) data and “C” segments according to Menegatti et al. (1998), Oceanic Anoxic Event 1a (OAE1a; shaded in gray), and magnetostratigraphy (VPDB—

Vienna Peedee belemnite; Nanno.—Nannofossil zones). Level of the U-Pb date (in red; Corfu et al., 2013) in the DH1 core is projected from two nearby bentonite-bearing cores (DH3 and DH7) with well locations shown in the location map (D). VGP—virtual geomagnetic pole; lat.—latitude; ChRM—characteristic remanent magnetization; inc.—inclination.

4. 氧同位素示踪地球最早陆壳的起源



翻译人：冯婉仪 fengwy@sustech.edu.cn

Smithies R H, Lu Y J, Kirkland C L, et al. *Oxygen isotopes trace the origins of Earth's earliest continental crust*[J]. *Nature*, 2021, 592: 70-74.

<https://doi.org/10.1038/s41586-021-03337-1>

摘要：现今地球大部分陆壳是在太古代末期（25 亿年前）形成的。在大约 25-50 公里深处，通过含水玄武质岩石的熔融，形成一系列英云闪长岩-奥长花岗岩-花岗闪长岩（TTG）的钠质花岗岩。然而，其所涉及的地球动力学背景和过程仍存在争议，并且产生了一些根本性的问题，如：所需的水是如何以及从哪里加入到地壳深部 TTG 源区的。此外，目前还没有大量均匀的、富集足够多不相容微量元素以至于能作为 TTG 源区的玄武岩序列保存在太古宙地壳中的报道。在此，我们利用锆石氧同位素组成的变化和全岩石地球化学识别了两组不同的 TTG。强烈钠化的 TTG 代表了最原始的岩浆，其含有的锆石的氧同位素组成反映了源岩已被原始幔源水水化。这些原始的 TTG 不需要一个像“平均”TTG 那样富含不相容微量元素的源区。相比之下，“演化”的较低钠化的 TTG 需要一个富集来自水圈的水和不相容微量元素的源区，其中这些不相容微量元素与由交代的地幔岩石圈熔融形成的含水岩浆（赞岐岩）的加入有关。通过集中研究来自 Pilbara 克拉通古太古代地壳的数据，我们可以忽略俯冲的背景，而认为含水且富集的近地表玄武岩是通过密度驱动的地壳对流翻转进入地幔的。这些结果消除了许多在理解早期大陆地壳形成过程中自相矛盾的障碍。我们的研究表明，足够多的原始水已经存在于地球早期的镁铁质地壳中以至于产生了大陆的原始核，并且通过早期地球特有的动态过程产生了额外的含水源区。

ABSTRACT: Much of the current volume of Earth's continental crust had formed by the end of the Archaean eon¹ (2.5 billion years ago), through melting of hydrated basaltic rocks at depths of approximately 25–50 kilometres, forming sodic granites of the tonalite–trondhjemite–granodiorite (TTG) suite^{2–6}. However, the geodynamic setting and processes involved are debated, with

fundamental questions arising, such as how and from where the required water was added to deep-crustal TTG source regions^{7,8}. In addition, there have been no reports of voluminous, homogeneous, basaltic sequences in preserved Archaean crust that are enriched enough in incompatible trace elements to be viable TTG sources^{5,9}. Here we use variations in the oxygen isotope composition of zircon, coupled with whole-rock geochemistry, to identify two distinct groups of TTG. Strongly sodic TTGs represent the most-primitive magmas and contain zircon with oxygen isotope compositions that reflect source rocks that had been hydrated by primordial mantle-derived water. These primitive TTGs do not require a source highly enriched in incompatible trace elements, as 'average' TTG does. By contrast, less sodic 'evolved' TTGs require a source that is enriched in both water derived from the hydrosphere and also incompatible trace elements, which are linked to the introduction of hydrated magmas (sanukitoids) formed by melting of metasomatized mantle lithosphere. By concentrating on data from the Palaeoarchaean crust of the Pilbara Craton, we can discount a subduction setting^{6,10-13}, and instead propose that hydrated and enriched near-surface basaltic rocks were introduced into the mantle through density-driven convective overturn of the crust. These results remove many of the paradoxical impediments to understanding early continental crust formation. Our work suggests that sufficient primordial water was already present in Earth's early mafic crust to produce the primitive nuclei of the continents, with additional hydrated sources created through dynamic processes that are unique to the early Earth.

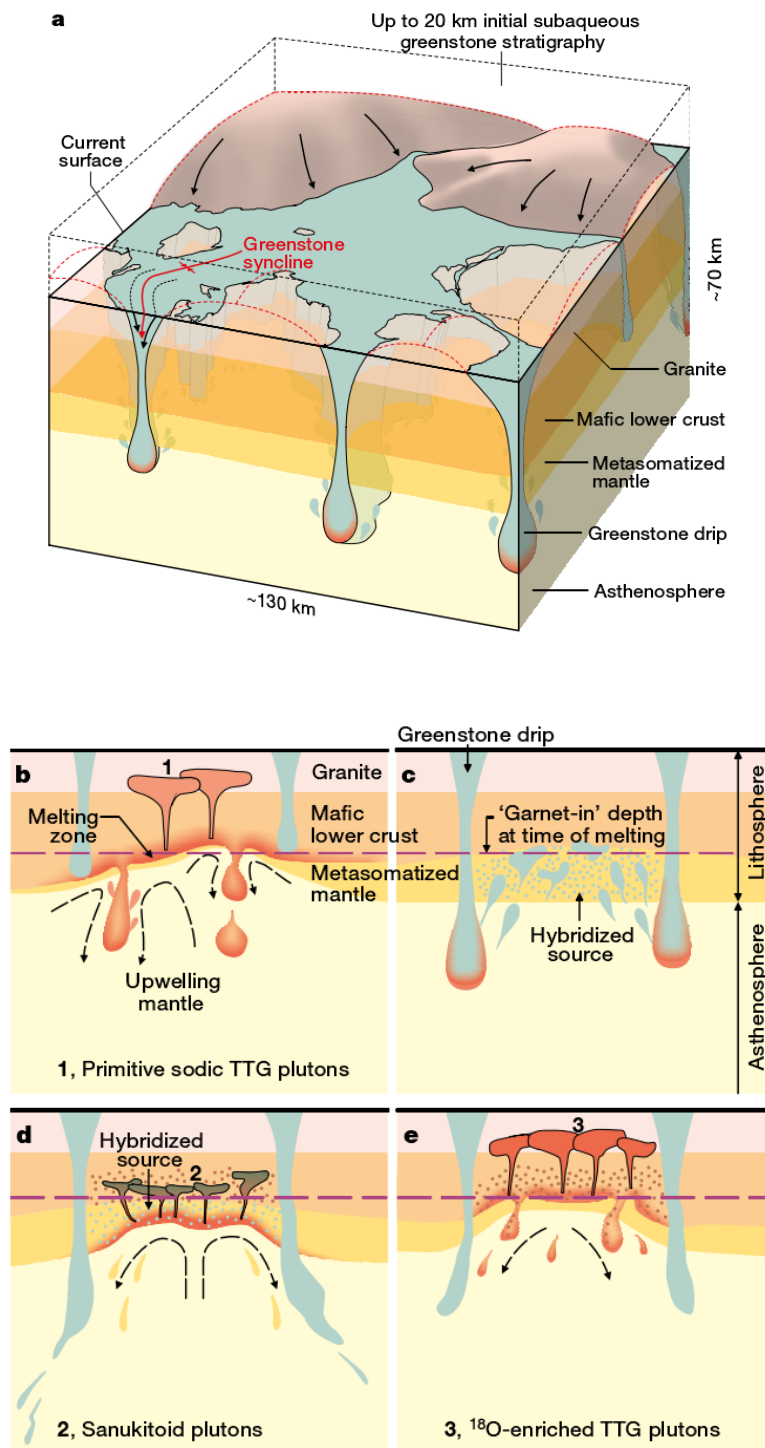


Figure 1. Forming Earth's early felsic crust. a, Illustration depicting continuous gravity-driven dripping of ^{18}O -enriched greenstones through the entire crustal column and into the mantle. b, Primitive Pilbara TTG indicates that the earlier Archaean mafic lower crust was already at least locally hydrated enough in low ^{18}O mantle-derived water to undergo partial melting during periods of lithospheric extension and

dripping. Lower crustal drips may have caused limited metasomatic enrichment of lithosphere, augmenting the trace-element inventory of TTG sources. c, Greenstone that dripped into the mantle released ^{18}O -enriched fluids and hydrated partial melts that metasomatized the lithospheric mantle. d, Under extension, the metasomatized lithospheric mantle melted to produce large-ion lithophile element-enriched, Th-enriched and light rare earth element-enriched sanukitoid, containing > 7 wt% dissolved H_2O (ref. 48). e, In turn, the enriched sanukitoid infiltrated and mingled with ductile mafic lower crust to form the hybridized source for ^{18}O -enriched TTG. Although addition of only ~ 17% sanukitoid to the lower mafic crust satisfies the enriched trace-element source requirements of ^{18}O -enriched TTG, mass-balance calculations (see Methods) require that at least 40% of the oxygen in that source came from greenstone drips, indicating that upon crystallization, sanukitoid magmas also exsolved large volumes of ^{18}O -enriched fluids that pervasively hydrated the evolving TTG sources.

5. 俯冲持续时间和板片倾斜



翻译人：刘伟 ineway@163.com

Hu J., & Gurnis M. *Subduction Duration and Slab Dip* [J]. *Geochemistry Geophysics Geosystems*, 2020, 21(4).

<https://doi.org/10.1029/2019GC008862>

摘要：板片倾斜是俯冲带最明显的特征之一，但控制它们的因素仍然不清楚。在这里，我们通过分析世界各地的俯冲带的 153 条断面获得了板片的倾角和俯冲参数，包括俯冲持续时间、上覆板块的性质、板块年龄和汇聚速度。根据同位素确定的弧形成年龄以及俯冲形成的地层、构造、板块构造和地震等指示，给出了俯冲持续时间的综合分析表。我们提出了两个俯冲带的年龄，一个是长期年龄，一个是再启动年龄。通过相互关系和多元回归分析，我们发现：(1)俯冲时间是控制板片倾角的主要参数，在俯冲时间较长的区域，板片倾向于更浅的倾角；(2)俯冲持续时间的长期年龄比再启动年龄更能解释浅层倾角的变化；(3)上覆板块的性质可能会影响浅层倾角的角度，大陆下面的板片往往倾向于更浅的倾角；(4)板片年龄对板片倾角有影响，年轻板片有更陡的浅层倾角；(5)板片倾角与俯冲参数之间的相关性与深度有关，俯冲持续时间和上覆板块性质解释这一关系的能力随着深度的增加而减弱。我们的分析强调了俯冲历史和俯冲带的长期区域状态对确定板块倾角的重要性，并与俯冲力学模型一致。

ABSTRACT: The dip angles of slabs are among the clearest characteristics of subduction zones, but the factors that control them remain obscure. Here, slab dip angles and subduction parameters, including subduction duration, the nature of the overriding plate, slab age, and convergence rate, are determined for 153 transects along subduction zones for the present day. We present a comprehensive tabulation of subduction duration based on isotopic ages of arc initiation and stratigraphic, structural, plate tectonic and seismic indicators of subduction initiation. We present two ages for subduction zones, a long - term age and a reinitiation age. Using cross correlation and

multivariate regression, we find that (1) subduction duration is the primary parameter controlling slab dips with slabs tending to have shallower dips at subduction zones that have been in existence longer; (2) the long - term age of subduction duration better explains variation of shallow dip than reinitiation age; (3) overriding plate nature could influence shallow dip angle, where slabs below continents tend to have shallower dips; (4) slab age contributes to slab dip, with younger slabs having steeper shallow dips; and (5) the relations between slab dip and subduction parameters are depth dependent, where the ability of subduction duration and overriding plate nature to explain observed variation decreases with depth. The analysis emphasizes the importance of subduction history and the long - term regional state of a subduction zone in determining slab dip and is consistent with mechanical models of subduction.

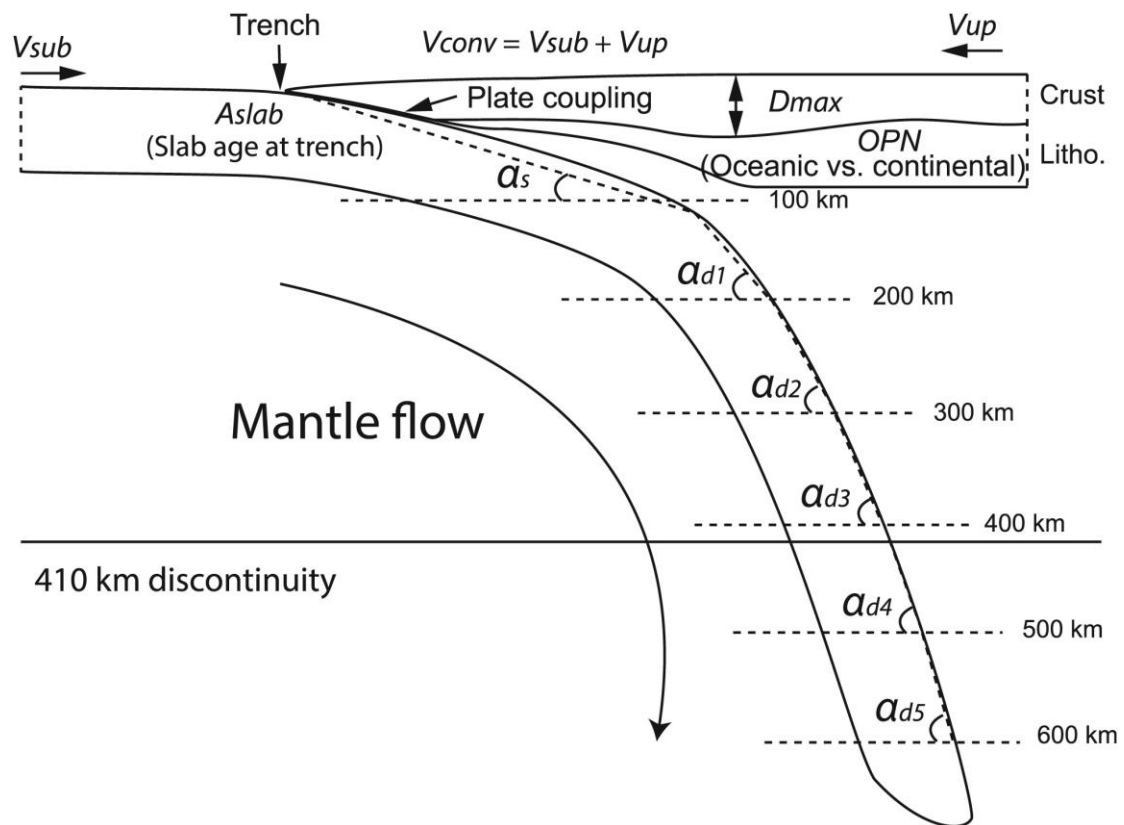


Figure 1. Schematic representation of slab dips and subduction parameters. The subducting plate rate V_{sub} , convergence rate V_{conv} , and the rate of upper plate motion V_{up} are all positive toward the trench. Only the trench - normal components of these parameters are used in the study. The maximum Moho depth D_{max} is measured within 300 km from the trench. α_s is shallow dip; α_d is deep dip; OPN is overriding plate nature; and A_{slab} is slab age at trench.

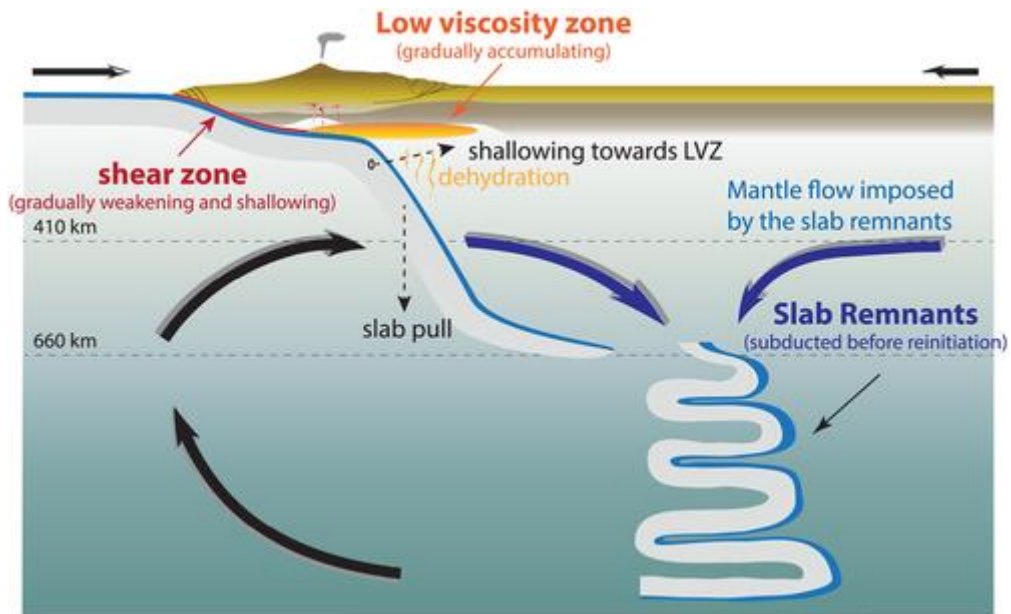


Figure 2. Long - term state of the subduction zone, where the slab remnants (from earlier subduction), the low viscosity zone at shallow depth, and the shear zone at the plate interface inherited from earlier subduction contribute to the shallowing of the new slab.

6. 气候稳定性定义的东亚季风区的全新世气候适宜期



翻译人：杨会会 11849590@mail.sustech.edu.cn

Zhang Z P, Liu J B, Chen J, et al., *Holocene climatic optimum in the East Asian monsoon region of china defined by climatic stability*[J].*Earth-Science Reviews*,2021,212,103450

<https://doi.org/10.1016/j.earscirev.2020.103450>

摘要：全新世气候适宜期（HCO）在整个东亚季风区是否是同步发生的还没有定论，如果是同步发生的，那么是发生在早全新世（EH, 11.7-8.0 ka）还是发生在中全新世（MH, 8.0-4.0 ka）？这是因为之前古气候研究对 HCO 的定义主要基于温度的最大值或者温度和降水相结合的最适宜期。由于史前文明的发展和人类福利与气候变化息息相关，从气候稳定性的角度来定义 HCO 或许更有意义，而这将为 HCO 发生时间的争论提供一个新的视角。本文中我们通过弦距法（SCD）来定量化比较 EH 和 MH 的气候稳定性，其中，弦距法是一种量化时间序列中样本方差的时间差异的有效方法，而这种比较是基于在东亚季风区与东亚夏季风相关的古气候指标的差异范围。研究结果表明弦距值（SCD 值）从早全新世到中全新世显著降低，指示一种更稳定的气候，这在中全新世的东亚季风区同步发生。我们认为中全新世的稳定气候为农业和畜牧业的发展提供了优越的环境，这有利于人口的迅速增加和仰韶文化的繁荣，仰韶文化是中国东亚季风区在全新世最繁荣的新石器时代文明。所以，我们认为中全新世稳定的气候可以被用来定义东亚季风区同时性的全新世气候适宜期（HCO），这时期社会发展和人口增长比全新世早期更好。TraCE-21 ka 气候模型揭示了随着北半球冰盖的消退，西风急流的变化从早全新世到中全新世明显减弱，而西风急流目前正被大尺度冰盖干扰。西风急流在中全新世的减弱，通过东亚夏季风和西风急流的相互作用增强了东亚季风区气候的稳定性。

ABSTRACT: It is unclear whether the Holocene climatic optimum (HCO) occurred synchronously throughout the East Asian summer monsoon (EASM) region, and if it did, whether it occurred in

the early Holocene (EH, 11.7–8.0 ka, ka = 1000 years before present, where the “present” is defined as the year CE 1950), or in the middle Holocene (MH, 8.0–4.0 ka). This is because the definition of the HCO in previous paleoclimatic studies was mainly based on the criterion of maximum temperature or some “optimum” combination of temperature and precipitation. Since the development of prehistoric societies and human welfare are closely linked to climatic variability, it may be more meaningful to define the HCO from the perspective of climatic stability, which may provide fresh insight into the debate on the timing of the HCO. Here we use calculations of squared chord distance (SCD), an effective method for quantifying temporal dissimilarity of the variance of samples in a time series, to quantitatively compare the climatic stability of the EH and the MH, based on a diverse range of the EASM-associated paleoclimatic records from the EASM region. The results show that the SCD values decreased significantly from the EH to the MH, indicating a more stable climate which occurred synchronously during the MH in the EASM region. We suggest that the stable climate of the MH provided an optimum environment for the development of agriculture and animal husbandry, which contributed to rapid population growth and the flourishing of the Yangshao culture which was the most prosperous Neolithic culture in the EASM region of China during the Holocene. Thus we propose that the stable MH climate can be used to define a synchronous HCO of the EASM which was more supportive of societal development and population growth than that during the EH. The results of TraCE-21 ka climatic modeling reveal that, with the retreat of the Northern Hemisphere ice sheets, the variability of the westerly jet (WJ), which was previously perturbed by large ice sheets, was significantly reduced from the EH to the MH. This reduced WJ variability during the MH enhanced the stability of the climate of the EASM region, via the interactions of the EASM and the WJ.

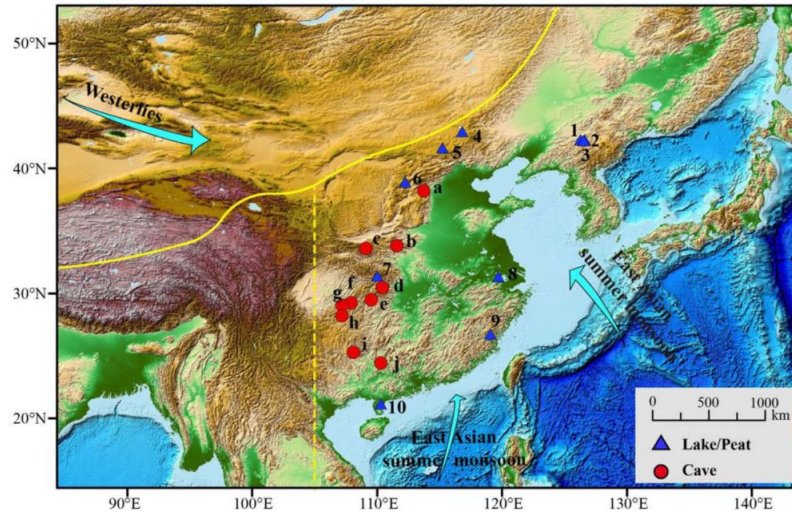


Figure 1. Locations of monsoon-related paleoclimatic records from the EASM region used in this study, including from lake sediments and peats (blue triangles) and stalagmites (red circles). 1, Gushantun Peatland; 2, Sihailongwan Lake; 3, Hani Peatland; 4, Haolaihure paleolake; 5, Bayanchagan Lake; 6, Gonghai Lake; 7, Dajiuhu Peatland; 8, Xinjie; 9, Shuizhuyang Peatland; 10, Huguangyan Maar Lake. a, Lianhua Cave; b, Dongshiya Cave; c, Jiuxian Cave; d, Heshang Cave; e, Lianhua Cave; f, Furong Cave; g, Jinfo Cave; h, Shigao Cave; i, Dongge Cave; j, Fengyu Cave. (Additional information is given in Table 1, Table 2). The main trajectories of the westerlies and the EASM are indicated by arrows. The modern northern limit of the Asian summer monsoon is shown by a yellow line (Chen et al., 2008). The vertical dashed line at 105°E longitude line represents the approximate boundary between the regions influenced by the ISM and the EASM (Gao et al., 1962; Wang et al., 2003, Wang et al., 2008a). (For interpretation of the references to colour in this figure legend, the reader is referred to the web version of this article.)

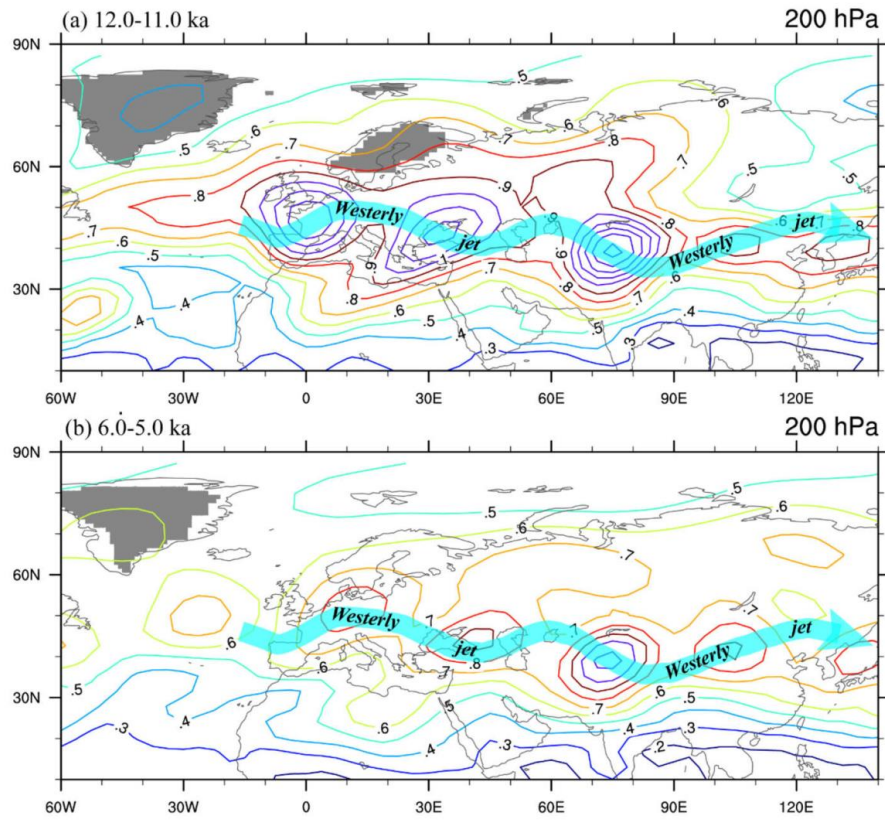


Figure 2. Spatial distribution of the standard deviation of meridional wind at 200 hPa during (a) the early Holocene, 12–11 ka, and (b) the middle Holocene, 6–5 ka. The area of Northern Hemisphere ice sheets at (a) 12 ka and (b) 6 ka are shown in gray.

7. 利用硅藻和生产力参数推断 172 ka 以来白令海西部的轨道和亚轨道环境变化



翻译人: 王浩森 11930841@mail.sustech.edu.cn

Gorbarenko S, Malakhova G. *Orbital and suborbital environmental changes in the Western Bering Sea during the last 172 ka Inferred from Diatom and Productivity Proxies*[J]. *Global and Planetary Change*, 2021, 198: 103405.

<https://doi.org/10.1016/j.gloplacha.2020.103405>

摘要: 硅藻的丰度和种类分布为重建 172 ka 时期西南白令海的轨道和千年-百年尺度气候和环境变化提供了一个精细的工具, 此外还有生产力指标 (氯, 颜色 b^* 和 Ca/Ti) 比值, 磁化率和生物标记参数, 这些参数是本文在 Shirshov Ridge (MSR) 中部得到的岩芯 SO201-2-85KL 得出的。现有数据表明, 在冷期, MIS 6.5-2, MSR 地区受到明显的季节性海冰影响。在 MIS 2 较冷的过程中, 主要的冰消区向 MSR 的南侧延伸, 可能在海面之外, 而在最冷的 MIS 6.2, 由于阿留申低压向西伯利亚东部的转移, MSR 区域没有结冰, 并且暴风雨的潮湿温暖空气向北转移到白令海西部。在暖期的 MIS 5.5, MSR 地区的海冰影响可以忽略不计, 几乎与全新世相同, 并且在事件 26 (120.5 ka) 之后开始增加。硅藻丰度及其物种分布的千年尺度变化是由格陵兰冷暖期交换期生产力的变化来触发的。硅藻的物种分布显示出 MSR 环境变化的复杂模式, 这与 Dansgaard -Oeschger 旋回中格陵兰岛气温的千年至百年变化一致。它证实了在这些偏远地区之间千年至百年时间尺度上的快速的大气遥相关机制。

ABSTRACT: Diatom abundance and species distribution present a subtle tool for the reconstruction of the orbital and millennial-centennial climate and environmental changes in the southwestern Bering Sea during the last 172 ka, in addition to productivity proxies (chlorine, color b^* , and Ca/Ti ratio), magnetic susceptibility, and biomarker proxies derived earlier and in this paper from the sediment core SO201-2-85KL recovered at the middle Shirshov Ridge (MSR). Available data indicate that the MSR area undergoes a significant seasonal sea ice influence during cold MISs 6.5–2. During the colder MIS 2, a main area of ice discharge extended southward of the MSR, likely

outside of the sea, while over the coldest MIS 6.2, the MSR area was free from ice due to the shifting of the Aleutian Low to the eastern Siberian coast and the northward transfer of the warm and wet air of storm tracks into the western Bering Sea. During the warm MIS 5.5, the sea ice influence at the MSR area was negligible, nearly the same as it was over the Holocene, and it began to increase after event 26 (120.5 ka). The millennial scale variability of diatom abundance and its species distribution were triggered by Greenland Interstadials accompanied by productivity changes. The diatom species distribution showed complicated pattern of variability of the MSR environment, consistent with the millennial-centennial changes of the Greenland air temperature over the Dansgaard-Oeschger cycles. It confirms the rapid mechanisms of atmospheric teleconnection between these remote regions on the millennial-centennial time scale.

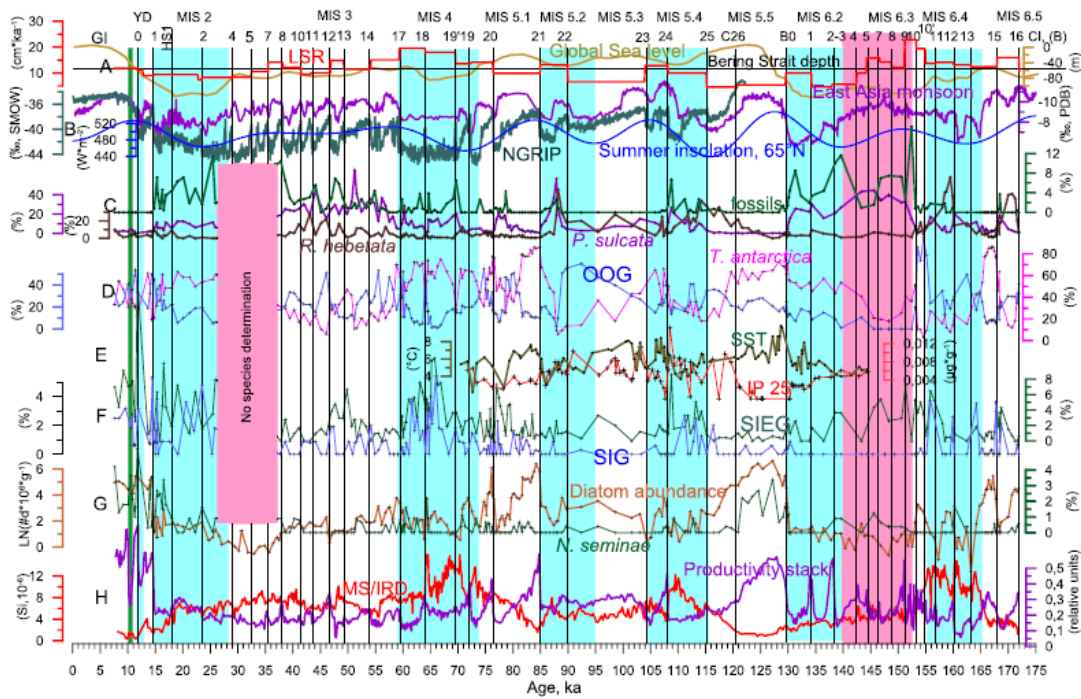


Figure 1. Orbital- and millennial-scale changes of the middle Shirshov Ridge environment during the last 172 ka. A. Relative sea level (Waelbroeck et al. 2002) and linear sedimentation rate. B. $\delta^{18}\text{O}$ of the Greenland NGRIP ice core (NGRIP members, 2004) on the GICC05 timescale (Rasmussen et al. 2006), $\delta^{18}\text{O}$ of the Hulu and Sanbao cave stalagmites (Wang et al. 2008), and Northern Hemisphere summer insolation at the 65°N (Berger 1978). Numbers of the MISs and the Greenland and Chinese interstadials are shown at the top. C. Percentages of *P. sulcata* and *R. hebetata*. D. Percentages of open ocean group (OOG) and *T. antarctica*. E. Biomarkers SST and IP 25 (Max et al., 2014). F. Percentages of sea ice edge

(SIEG) and sea ice (SIG) groups. G. DA and % of *N. seminae*. H. Stack of productivity and MS. The cold MISs and substages are marked by blue bars. Pink rectangles denote the periods with very low values of DA. Green bar indicate tephra layer over the Holocene. (For interpretation of the references to color in this figure legend, the reader is referred to the web version of this article.)

8. 第一个成冰纪的古强度结果及其对内核成核年龄的潜在意义



翻译人：张伟杰 12031188@mail.sustech.edu.cn

Lloyd SJ, Biggin AJ, Halls H, et al. *First palaeointensity data from the cryogenian and their potential implications for inner core nucleation age [J]. Geophysical Journal International, 2021, 226(1):66-77.*

<https://doi.org/10.1093/gji/ggab090>

摘要：地核成核时间是地球演化过程中一个非常重要的事件，一直是人们激烈争论的话题。一些最新理论估计地核的成核年龄是在新元古代，比之前想象的要年轻得多。一个年轻的内核需要更快的近期内核冷却速度和一个可能更热的早期内核。了解它的年龄对于了解地球的热历史和总能量是非常宝贵的。数值发电机模型生成的预测需要用这些数据进行测试，但目前记录太少，无法将事件限制在一个精确的时间段内。本文，我们展示了来自富兰克林大火成岩省的 720 Ma 辉绿岩岩脉(和一个岩床)的结果，这些岩脉的古强度结果处于至关重要的没有数据 300 Myr 范围内。本研究使用三种独立的技术对分布在加拿大和格陵兰高纬度北极地区的 11 个采样点的全岩样品进行研究，产生的虚偶极矩的范围为 5-20 ZAm² (平均 11 ZAm²)。几乎比现在的磁场低一个数量级。这些弱场结果与 150 万年后埃迪卡拉纪岩石得到的超低古强度数据一致，可能支持地磁发电机在年轻的内核形成之前新元古代就处于崩溃的边缘。

ABSTRACT: The timing of inner core nucleation is a hugely significant event in Earth's evolution and has been the subject of intense debate. Some of the most recent theoretical estimates for the age of nucleation fall throughout the Neoproterozoic era; much younger than previously thought. A young inner core requires faster recent core cooling rates and a likely hotter early core; knowledge of its age would be invaluable in understanding Earth's thermal history and total energy budget. Predictions generated by numerical dynamo models need to be tested against such data, but records

are currently much too sparse to constrain the event to a precise period of time. Here, we present results from 720 Ma dolerite dykes (and one sill) from the Franklin Large Igneous Province, which fall within a crucial 300 Myr gap in palaeointensity records. This study uses three independent techniques on whole rocks from 11 sites spread across High Arctic Canada and Greenland to produce virtual dipole moments ranging from 5 to 20 ZAm² (mean 11 ZAm²); almost one order of magnitude lower than the present-day field. These weak-field results agree with recent ultralow palaeointensity data obtained from Ediacaran rocks formed ~150 Myr later and may support that the dynamo was on the brink of collapse in the Neoproterozoic prior to a young inner core formation date.

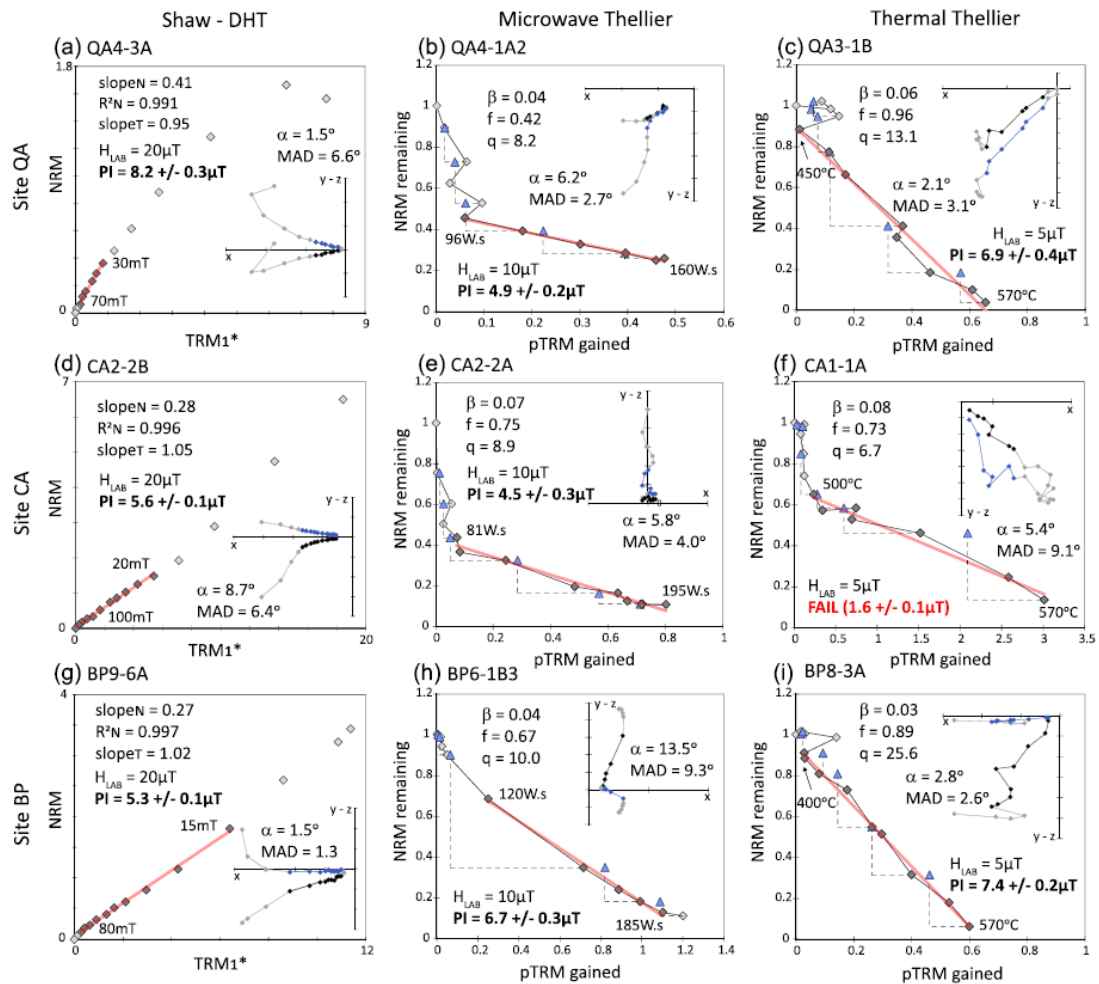


Figure 1. A selection of Arai plots from the microwave and thermal Thellier experiments, and Shaw pseudo-Arai plots (units 10⁻⁶ Am²). Each column includes only results from the same method; each row includes only results from the same site. CA2-2A and CA2-2B are sister specimens. Red line, best-fitting

line for palaeointensity points used; blue triangles, pTRM checks; dashed lines, link the pTRM check to the position that the check was carried out. Dark grey points are used in palaeointensity determination; light grey points are not used. Orthogonal plot data corresponding to (pseudo)-Arai plots are highlighted in black and blue with the remaining points greyed out. An explanation of the selection criteria is given in Section 3.2.

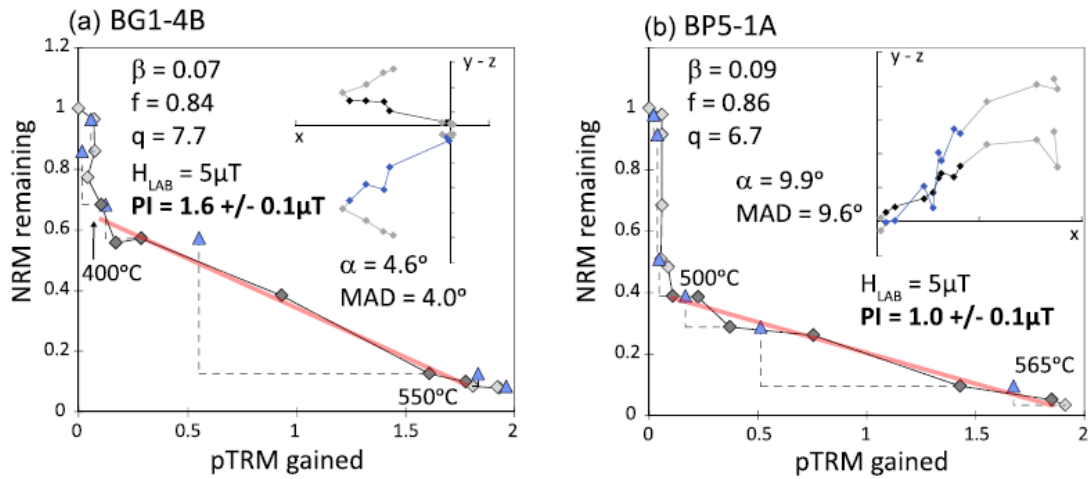


Figure 2. (a and b) Additional thermal Thellier Arai diagrams with associated orthogonal plots. See selection criteria (Section 3.2) and caption in Fig 4 for further details.

9. 洞穴沉积物记录了中心更新世格陵兰东北部温暖湿润的气候



翻译人：李海 12031330@mail.sustech.edu.cn

Moseley, G.E, Edwards, R.L, Lord, N.S, et al. *Speleothem record of mild and wet mid-Pleistocene climate in northeast Greenland*[J]. *Science Advances*, 2021, 7, eabe1260.

<https://doi.org/10.1126/sciadv.abe1260>

摘要:通常认为中布容事件 (~430 ka) 前的 5 次间冰期比中布容事件后的冷。但存在区域不均匀性, 表明北极地区在 MIS 15a 阶段比现今温暖。作者最先使用北极地区的洞穴沉积物记录研究 588 ka ~ 549 ka 格陵兰东北部的气候演化。结果显示, 与现今相比气温至少增加了 3.5°C, 导致冻土融化和降水增多。降水中 $\delta^{18}\text{O}$ 的值比现今至少高出 3‰, 淡水的输入引起两次区域性降温事件。研究结果对于增进对引起 MBE 的区域气候响应的理解具有重要意义, 尤其是为北极变暖的气候响应提供见解。

ABSTRACT: The five interglacials before the Mid-Brunhes Event (MBE) [c.430 thousand years (ka) ago] are generally considered to be globally cooler than those post-MBE. Inhomogeneities exist regionally, however, which suggest that the Arctic was warmer than present during Marine Isotope Stage (MIS) 15a. Using the first speleothem record for the High Arctic, we investigate the climatic response of northeast Greenland between c.588 and c.549 ka ago. Our results indicate an enhanced warmth of at least +3.5°C relative to the present, leading to permafrost thaw and increased precipitation. We find that $\delta^{18}\text{O}$ of precipitation was at least 3‰ higher than today and recognize two local cooling events (c.571 and c.594 ka ago) thought to be caused by freshwater forcing. Our results are important for improving understanding of the regional climatic response leading up to the MBE and specifically provide insights into the climatic response of a warmer Arctic.

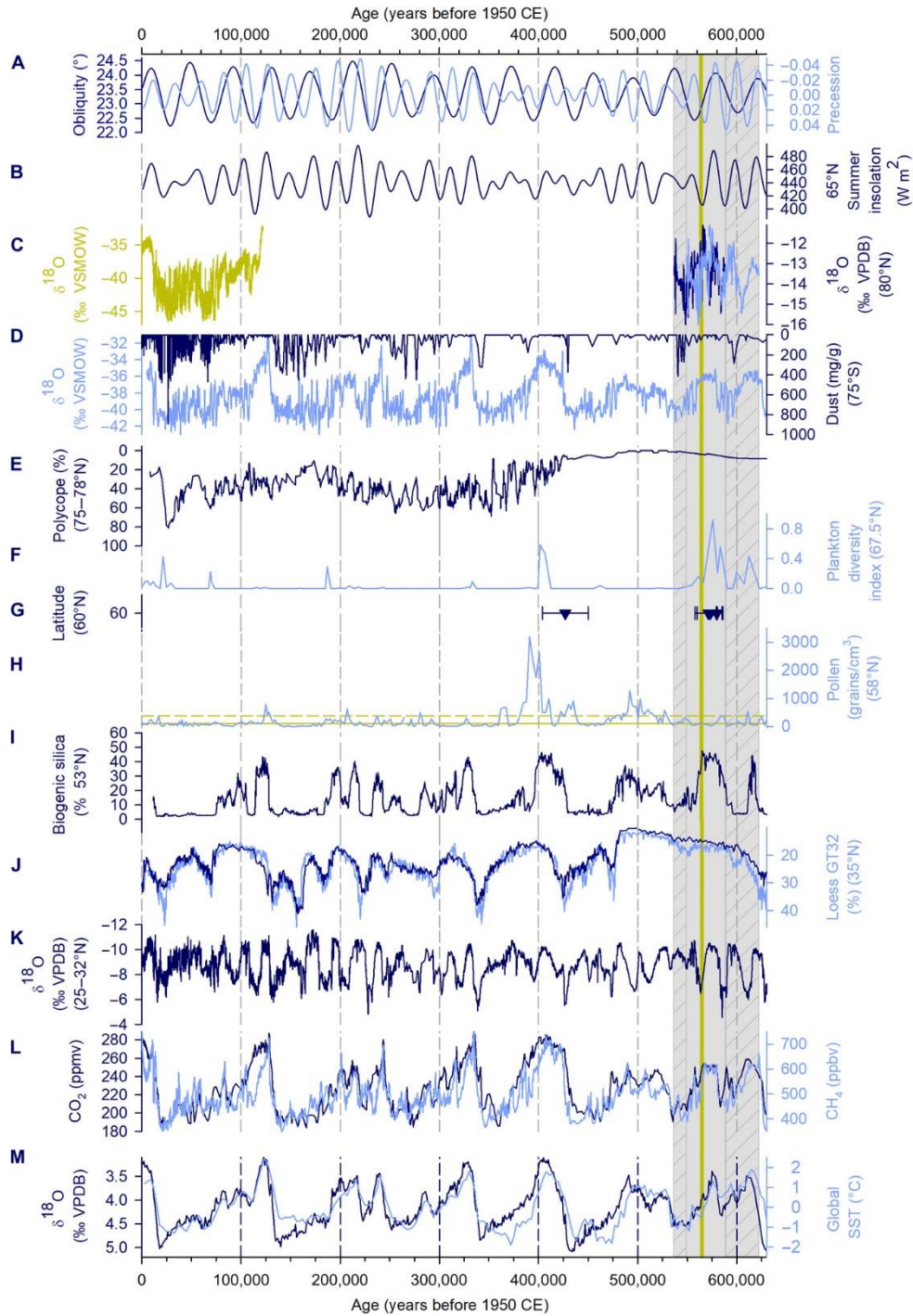


Figure 1. Greenland speleothem $\delta^{18}\text{O}$ record compared with other paleoclimate archives for the period 0 to 630 ka ago. (A) Obliquity (dark blue) (73) and precession (light blue) (73). (B) The 65°N summer insolation (73). (C) NGRIP Greenland $\delta^{18}\text{O}$ record (dark yellow) (74). U-Th-based (dark blue) and orbitally refined (light blue) age models for 80.2°N Greenland speleothem $\delta^{18}\text{O}$ record (this study). (D) Synthetic Greenland $\delta^{18}\text{O}$ record (light blue) (34). EPICA Dome C (EDC) atmospheric dust (dark blue) (40). (E) Arctic Ocean Polycyope abundance (39). (F) Lake El'gygytyn plankton diversity index (10).

(G) Eastern Siberian speleothem ages (36). (H) South Greenland marine pollen record (37). Solid yellow horizontal bar indicates Holocene baseline. Dashed yellow horizontal bar indicates MIS 15a baseline. (I) Lake Baikal biogenic silica record (9). (J) Chinese loess grain size $>32 \mu\text{m}$: Yimaguan (light blue) and Luoquan (dark blue) (43). (K) Asian monsoon composite speleothem record (33). (L) Atmospheric CO_2 (dark blue) (12–14) and CH_4 (light blue) (12, 13, 15) concentrations. (M) Global benthic $\delta^{18}\text{O}$ stack (dark blue) (41). Stacked global SST record (light blue) (44). Vertical gray bar highlights area of overlapping speleothem age models, with hatched vertical bars indicating only single age models. Vertical yellow line marks MIS 15a-14 boundary.

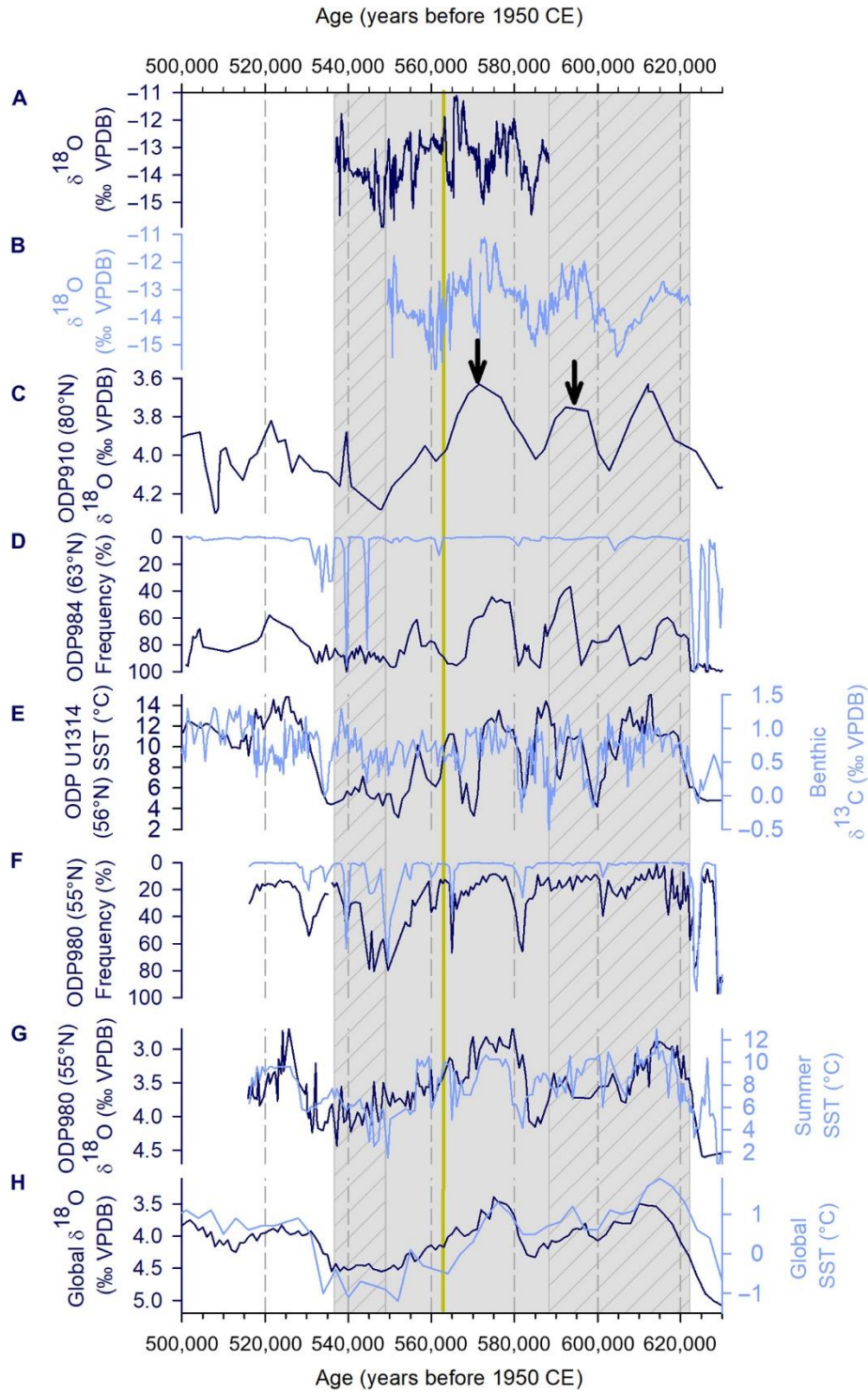


Figure 2. Greenland speleothem $\delta^{18}\text{O}$ record compared to marine records for the period 500 to 630 ka ago. (A) U-Th-based (dark blue) and (B) orbitally refined (light blue) age models for 80.2°N Greenland speleothem $\delta^{18}\text{O}$ record (this study). (C) ODP 910 80°N Arctic Gateway $\delta^{18}\text{O}$ planktic foraminifera record. Arrows indicate freshwater pulses (59). (D) ODP 984 63° N ice-rafted debris (light blue) and *N. pachyderma* (s.) abundance (dark blue) (45). (E) ODP U1314 56°N SST (dark blue) and benthic $\delta^{13}\text{C}$

(light blue) (46). (F) ODP 980 55°N ice-rafted debris (light blue) and *N. pachyderma* (s.) abundance (dark blue) (45). (G) ODP 980 55°N benthic foraminifera $\delta^{18}\text{O}$ (dark blue). Summer SST (light blue) (45). (H) Global benthic $\delta^{18}\text{O}$ stack (dark blue) (41). Stacked global sea surface temperature record (light blue) (44). Vertical gray bar highlights the area of overlapping speleothem age models, with hatched vertical bars indicating only single age models. Vertical yellow line marks the MIS 15a-14 boundary.

10. 裂谷火山活动和埃迪卡拉末期生物灭绝的联系：来自墨西哥 Sonora 地区地层学及 U-Pb 年代学综合研究



翻译人：周洋 zhouy3@sustech.edu.cn

Eben B. Hodgin, Lyle L. Nelson, Corey J. Wall et al. A link between rift-related volcanism and end-Ediacaran extinction? Integrated chemostratigraphy, biostratigraphy, and U-Pb geochronology from Sonora, Mexico [J]. Geology, 2021, 49:115–119.

<https://doi.org/10.1130/G47972.1>

摘要：我们对墨西哥 Sonora 岛横跨埃迪卡拉-寒武纪边界的地层剖面建立了生物地层学和年代学框架。富含赤铁矿的砂质白云岩地层的最大沉积年龄为 539.40 ± 0.23 Ma，位于记录了 La Ciénega 组内寒武纪基底碳同位素偏移最低点的碳酸盐岩上方 20 m 处。这一层包含了重新活化的凝灰岩，覆盖在最后一次出现埃迪卡拉动物化石的地层之上，而位于第一次出现痕迹化石 *Treptichnus pedum* 的寒武纪地层之下，因此该年龄为埃迪卡拉-寒武纪边界。很巧的是在 Laurentia 南部 ($> 250,000$ km³ 的玄武岩) 发育有同时代的裂谷玄武岩，碳同位素偏移为负，大火成岩省的爆发和埃迪卡拉生物大灭绝密切相关。

ABSTRACT: We present chemostratigraphy, biostratigraphy, and geochronology from a succession that spans the Ediacaran-Cambrian boundary in Sonora, Mexico. A sandy hematite-rich dolostone bed, which occurs 20 m above carbonates that record the nadir of the basal Cambrian carbon isotope excursion within the La Ciénega Formation, yielded a maximum depositional age of 539.40 ± 0.23 Ma using U-Pb chemical abrasion–isotope dilution–thermal ionization mass spectrometry on a population of sharply faceted volcanic zircon crystals. This bed, interpreted to contain reworked tuffaceous material, is above the last occurrences of late Ediacaran body fossils and below the first occurrence of the Cambrian trace fossil *Treptichnus pedum*, and so the age calibrates key markers of the Ediacaran-Cambrian boundary. The temporal coincidence of rift-related flood basalt volcanism in southern Laurentia ($>250,000$ km³ of

basalt), a negative carbon isotope excursion, and biological turnover is consistent with a mechanistic link between the eruption of a large igneous province and end-Ediacaran extinction.

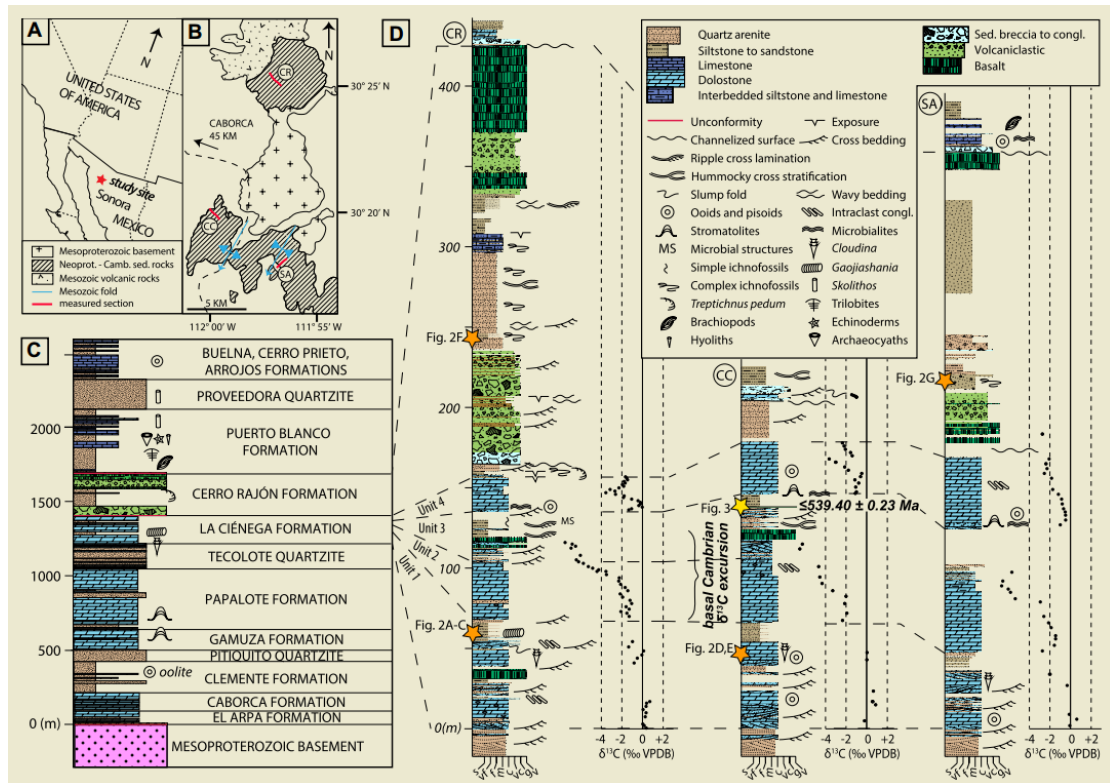


Figure 1. Locality map and integrated stratigraphy of the Ediacaran-Cambrian boundary near Caborca, northwestern Mexico. (A) Locality map with star marking the study site. (B) Geologic map showing distribution of Neoproterozoic–Cambrian strata and locations of measured sections; modified from Barrón-Díaz et al. (2019a). (C) Generalized Neoproterozoic–Cambrian lithostratigraphy and biostratigraphy, including data compiled from Stewart et al. (1984) and Barrón-Díaz et al. (2019a). (D) Integrated lithostratigraphy, biostratigraphy, $\delta^{13}\text{C}$ chemostratigraphy, and geochronology from measured sections, corresponding to Figure 1B. Neoprot.—Neoproterozoic; Camb.—Cambrian; CR—Cerro Rajón; CC—Cerro Clemente; SA—Cerro San Agustín; s—siltstone; vf—very fine-grained; f—fine-grained; m—medium-grained; c—coarse-grained; vc—very coarse-grained; g—conglomerate; v—volcanic; VPDB—Vienna Peedee belemnite; sed.—sedimentary; congl.—conglomerate.

11. 地球化学数据表明火星子午线平原的格拉斯伯格组和伯恩组地层的沉积物十分相似



翻译人：张琪 zhangq7@sustech.edu.cn

McCullom T M & Hyne B. *Geochemical data indicate highly similar sediment compositions for the Grasberg and Burns formations on Meridiani Planum, Mars [J]. Earth and Planetary Science Letters, 2021, 557, 116729.*

<https://doi.org/10.1016/j.epsl.2020.116729>

摘要：子午线平原伯恩组（Burns）含赤铁矿且富含硫酸盐的砂岩下面是一个薄的地层单元，被称为格拉斯伯格组（Grasberg）。含硫酸盐的格拉斯伯格组地层颗粒细，没有层理结构，此前根据其形态和化学性质的差异被认为是不同于上覆伯恩组的岩性单位。然而重新观测的数据表明，除 Mg、Ni、SO₃ 和 Mn 含量外，Grasberg 组和 Burns 组岩石的化学成分基本一致。Grasberg 组岩层相对较低的 Mg、Ni 和 SO₃ 含量表明它们经历了贫镁的硫酸盐成岩作用，与 Burns 组的 11 个亚地层岩石所缺乏的元素相似，其中包括紧靠 Grasberg 组上方的 2 个 Burns 组亚地层岩石。Grasberg 组和 Burns 组接触的地方在成岩过程中也明显缺乏 Mn。当补偿了成岩损失后，来自 Grasberg 组和 Burns 组的岩石具有几乎相同的化学成分，尽管 Grasberg 组岩石中的 SO₃ 含量要少一些。这些观察结果表明，Grasberg 组和 Burns 组的沉积物来源具有同源相关性，两组岩层在沉积后都经历了一些相同的成岩过程。此外，Grasberg 组地层和上覆的 Burns 组地层中 Mg、Ni、SO₃ 和 Mn 的明显损失，也反映在这些元素在下方 Shoemaker 组地层的裂缝中富集，表明在某些成岩事件中流体发生了向下运动。

ABSTRACT: The hematite-bearing, sulfate-rich sandstones of the Burns formation at Meridiani Planum are underlain by a thin stratigraphic unit referred to as the Grasberg formation. The sulfate-bearing Grasberg rocks are fine-grained and lack bedding structures, and were previously interpreted to be a distinct lithologic unit based on morphological and chemical differences from the overlying Burns formation. However, reanalysis of the data indicates that, except for variable

amounts of Mg, Ni, SO₃ and Mn, the chemical compositions of the Grasberg and Burns rocks are very similar. The relatively low levels of Mg, Ni, and SO₃ in the Grasberg rocks indicates that they have experienced diagenetic loss of Mg sulfates similar to that observed in a subset of eleven Burns formation rocks depleted in the same elements, including two Burns rocks immediately above the Grasberg contact. The Grasberg formation and Burns rocks near the contact have also evidently lost Mn during diagenesis. When compensated for diagenetic losses, rocks from the Grasberg and Burns formations are found to have nearly identical chemical compositions, albeit Grasberg rocks contained a few wt.% less SO₃. These observations suggest that the sediment sources for the Grasberg and Burns formations are genetically related, and that both formations experienced some of the same diagenetic processes after deposition. Furthermore, the apparent loss of Mg, Ni, SO₃, and Mn from the Grasberg formation and immediately overlying Burns rocks is mirrored by enrichments of these same elements in fractures within the underlying Shoemaker formation, suggesting downward movement of fluids during some diagenetic events.

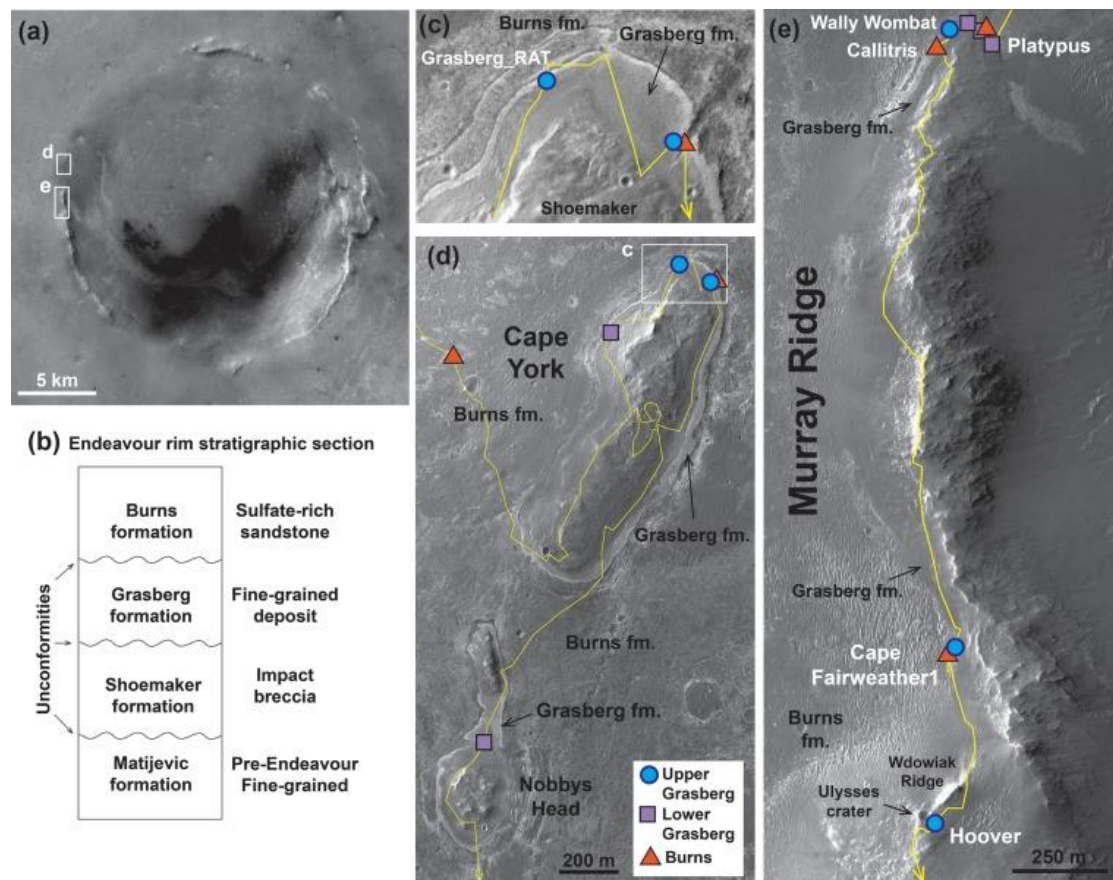


Figure 1. Overview of Endeavour crater area and prominent features. Yellow lines in (c-e) are the approximate rover track. Symbols show sites where targets from the Grasberg and Burns formations were

analyzed by the APXS, and targets discussed in the text are identified by white lettering. (a) Endeavour crater. Boxes outline areas shown in (d) and (e). (b) Stratigraphic section of rocks at rim of Endeavour (Arvidson et al., 2014; Crumpler et al., 2015). (c) North end of Cape York promontory. (d) Cape York area. (e) Murray Ridge area. Image sources: (a) Mars Reconnaissance Orbiter Context Camera (CTX) mosaic, NASA/JPL-Caltech/MSSS. (c-e) High Resolution Imaging Science Experiment image EPS_018846_1775_RED, NASA/JPL/University of Arizona. (For interpretation of the colours in the figure(s), the reader is referred to the web version of this article.)

12. 夏威夷近海淡水流的海洋电磁成像和体积估计



翻译人：张亚南 zhangyn3@mail.sustech.edu.cn

Eric A, Steven C, Dallas S, et al. *Marine Electromagnetic Imaging and Volumetric Estimation of Freshwater Plumes Offshore Hawai'i* [J]. *Geophysical Research Letters*, 2021, 48 (7), e2020GL091249.

<https://doi.org/10.1029/2020GL091249>

摘要：地下水溢流（SGD）是控制海陆过渡带水循环的重要现象。SDG 是一种从海底进入海水中的淡水流体，具有冰冷且有浮力的特征，包含着碳、营养物、金属离子和温室气体。也因此改变着沿海地区的海洋和生物化学性质。作者在文中展示了西夏威夷近海大尺度、高分辨率淡水流的电磁成像。利用电阻率模型反演发现了多个从海底到海表的垂直淡水流。此外，模型对广泛分布的淡水进行了空间成像。这些羽状流和表层淡水的电阻率在 1-30 Ωm 。通过电阻率—盐度的计算显示羽状流体的盐度在 0.3-9.9，含有高达 87% 的淡水。文中结果表明，在夏威夷近海中存在着大量的淡水水团。该研究为阐明水文地质和海洋过程对世界各地沿海水域生物地球化学的影响提供了一种全新的有效方法。

ABSTRACT: Submarine groundwater discharge (SGD) is an important phenomenon that governs hydrological cycles at the land - to - ocean transition zone. SGD manifests as cold and buoyant freshwaters influx from the seafloor to the water column that contains carbon, nutrients, metals, and greenhouse gases, altering coastal areas' oceanographical and biochemical properties. Here, we present electromagnetic imaging of large - scale freshwater plumes in high - resolution, offshore west Hawai'i. Electrical resistivity models detect multiple vertical freshwater plumes extending from the seafloor to the ocean surface. Additionally, our models image extensive spatially distributed surface freshwater. The resistivity of these plumes and surface freshwater ranges from ~ 1 to 30 Ωm . Resistivity - to - salinity calculation indicates a plume - scale salinity range of ~ 0.3 –9.9, containing up to 87% of freshwater. Our results imply that substantial volumes of freshwater

occupy water column plumes in Hawai'i. This study offers a new and effective method to elucidate hydrogeologic and ocean processes affecting biogeochemical cycles in coastal waters worldwide.

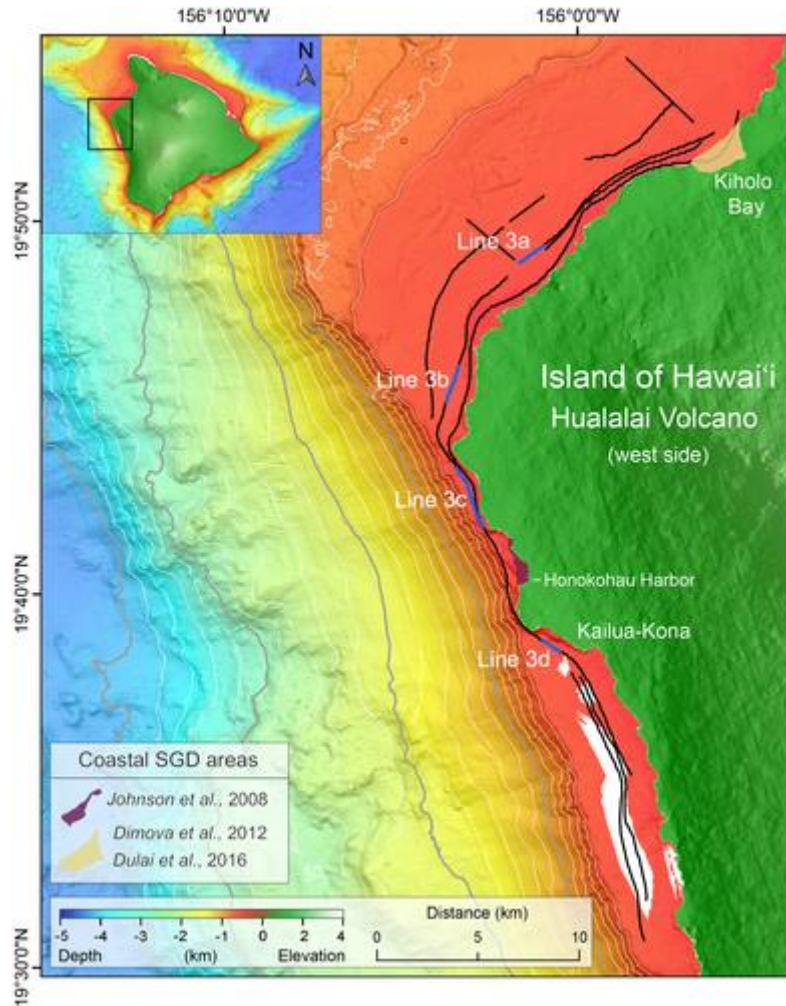


Figure 1. Map of the study area parallels the Hualalai terrestrial aquifer at Kailua-Kona, offshore west Hawai'i. The black lines denote the survey towlines (10 inlines and two crosslines). Blue lines represent regions where freshwater plumes were detected (Figures 2, 3, and S8). The purple and yellow polygons represent coastal SGD areas detected in previous studies. White lines denote depth contours of 200 m, and gray lines the depth contours of 1,000 m. Inset map: The island of Hawai'i, with a black rectangle indicating the main map area. The Hualalai terrestrial aquifer encompasses the entire map region. Areas with no bathymetry data are shown in white. Bathymetry data: Courtesy of Hawai'i Mapping Research Group.

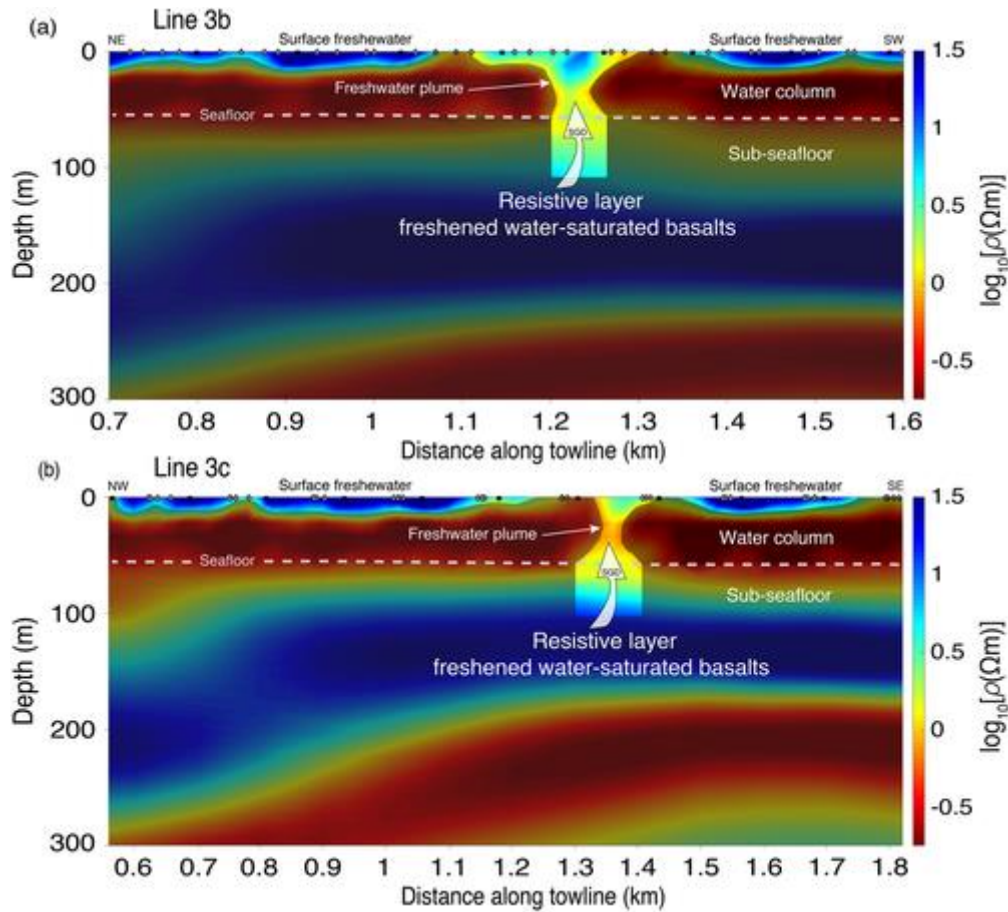


Figure 2. Two-dimensional inversion models derived from the CSEM data acquired in survey lines 3b and 3c. The color scale presents the electrical resistivity in $\log_{10}[\rho(\Omega\text{m})]$. Black squares and gray diamonds denote transmitter and receiver positions, respectively. (a) Line 3b inversion model. The gray dashed line represents the seafloor, positioned at a water depth of ~ 50 m. Resistive freshwater plume imaged at a towline distance of ~ 1.23 km. The plume is most likely fed by SGD (white arrow) sourced from the sub-seafloor layer of freshened water-saturated basalts. Two lateral resistive anomalies from both flanks of the model represent surface freshwater bodies. We note that for enhanced visibility of the water column resistive anomalies, the resistivity shading thresholds are set to $\sim 1.7 \Omega\text{m}$ and $\sim 6 \Omega\text{m}$ for the plume and surface freshwater bodies, respectively. This inversion converged to an RMS misfit of 1.0 after 12 iterations. The amplitude and phase data error floors are 8%. (b) Line 3c inversion model. Moderate freshwater plume detected at a towline distance of ~ 1.35 km. The shallow lateral resistive anomalies represent surface freshwater bodies that extend up to 700 m. The resistivity shading thresholds are set to $\sim 1 \Omega\text{m}$ and $\sim 6 \Omega\text{m}$ for the plume and surface freshwater bodies, respectively. This inversion fits an RMS misfit of 1.0 after 14 iterations, with error floors of 8% and 6% for the amplitude and phase data.

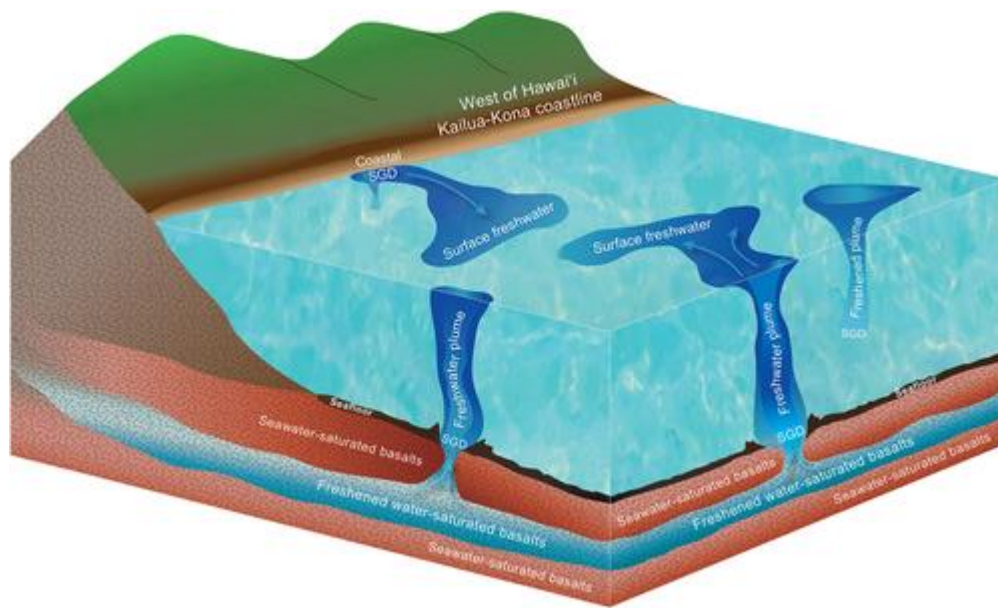


Figure 3. Conceptual model illustrating freshwater plumes and surface freshwater systems offshore west Hawai'i. Fresh groundwaters are transported from onshore to offshore through multilayer basaltic formation (Attias et al., 2020). From this sub-seafloor formation, freshened/freshwater migrate upward via porous/fractured seawater-saturated basalts, producing multiple large-scale vertical plumes that extend from the seafloor to the ocean surface. Surface freshwater bodies disconnected from plumes most likely result from nearby seeps or coastal SGD runoffs.